Electronic Supplementary Information

A Structurally Versatile Nickel Phosphite Acting as a Robust Bifunctional Electrocatalyst for Overall Water-Splitting

Prashanth W. Menezes,*[a] Chakadola Panda,[a] Stefan Loos,[b] Florian Bunschei-Bruns,[a] Carsten Walter,[a] Michael Schwarze,[a] Xiaohui Deng,[a] Holger Dau*[b] and Matthias Driess*[a]

[a] Department of Chemistry: Metalorganics and Inorganic Materials, Technische Universität Berlin, Straße des 17 Juni 135, Sekr. C2, 10623 Berlin, Germany

[b] Fachbereich Physik, Freie Universität Berlin, Arnimallee 14, 14195 Berlin, Germany

Chemicals

All chemical reagents (analytical grade) were used as received without any further purification. Commercially available nickel(II) chloride hexahydrate ($NiCl_2 \cdot 6H_2O$), ammonium dihydrogen phosphate ($NH_4H_2PO_4$), sodium hypophosphite (NaH_2PO_2), zinc powder (Zn), zinc (II) acetate dihydrate ($Zn(OAc)_2 \cdot 2H_2O$), sodium phosphate dodecahydrate ($Na_3PO_4 \cdot 12\ H_2O$) and potassium hydroxide (1 M KOH, Fe < 0.05 ppm determined by ICP-AES) solution were obtained from Sigma. Deionized water was used throughout the experiment.
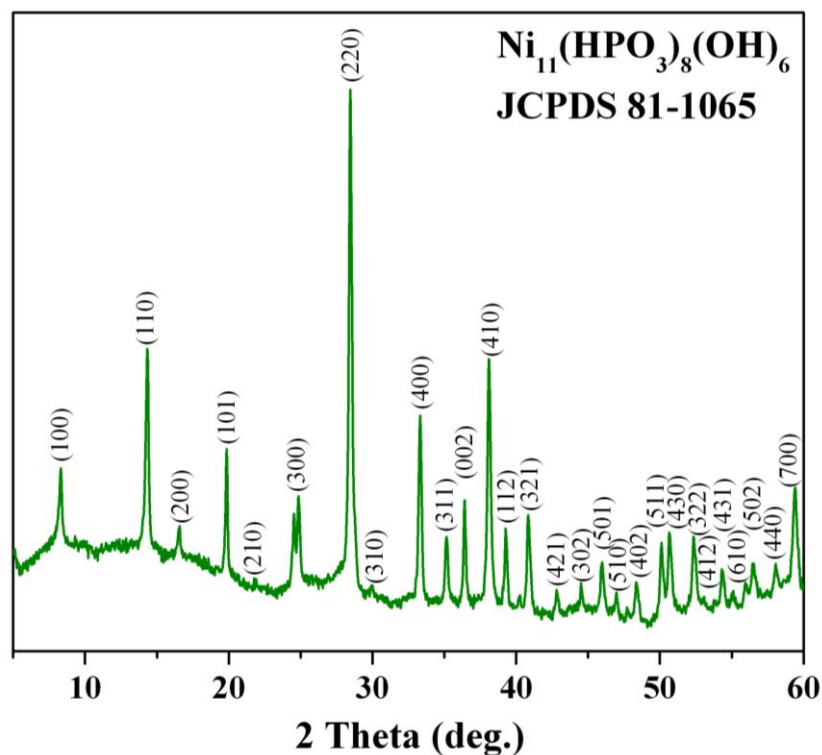

Figure S1. PXRD (in deg) and Miller indices (hkl) of as-prepared nickel phosphite, $Ni_{11}(HPO_3)_8(OH)_6$ (JCPDS 81-1065) synthesized via a mild hydrothermal approach.[1] The composition of Ni:P was additionally derived from EDX, ICP-AES and XPS.

Table S1. Determination of nickel and phosphorous ratio in nickel phosphite was obtained by ICP-AES and EDX Three independent measurements were performed for the reliability of the experiments and the average data is presented. In addition, the Ni:P composition on the surface was particles were derived from XPS analysis.

	Ni:P (Theoretical)	Ni:P (EDX)	Ni:P (ICP-AES)	Ni:P (XPS)
$Ni_{11}(HPO_3)_8(OH)_6$	1:0.72	~1:0.73	1:0.72	1:0.70
After OER CA	-	-	-	1:0.69
After HER CA	-	-	-	1:0.70

[001]

HPO$_3$
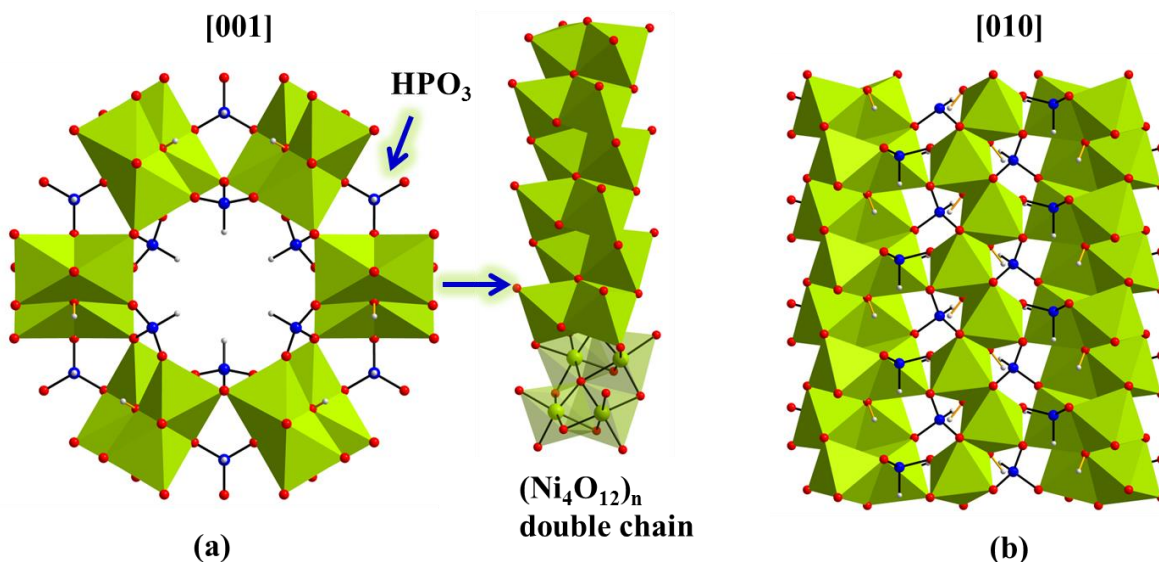
(Ni$_4$O$_{12}$)$_n$ double chain

(a)

[010]

(b)

Figure S2. Crystal structure and the building units of Ni$_{11}$(HPO$_3$)$_8$(OH)$_6$.[1-3] The crystal structure in the [001] direction is shown in (a). The crystal structure comprises of hexagonal arrangement where NiO$_6$ octahedron, where four oxygen atoms belong to (HPO$_3$)$^{2-}$ pseudo-tetrahedral and rest of the oxygen atoms belong to hydroxyl groups.[1-3] Interestingly, each of NiO$_6$ octahedron shares two of its edges with the next octahedron in the formation of (NiO$_4$)$_n$ zigzag chains. Condensation of equivalent four chains creates a (Ni$_4$O$_{12}$)$_n$ double chains along the *c*-axis. Linking of such (Ni$_4$O$_{12}$)$_n$ double chains by corner sharing results into three-dimensional octahedral arrays (c). Strikingly, two types of channels exist in the hexagonal arrangement formed by octahedra (highlighted in Figure 1). The smaller triangular channels, that are bound by three (Ni$_4$O$_{12}$)$_n$, are occupied by ¼ of the (HPO$_3$)$^{2-}$ pseudo-tetrahedral groups whereas the other ¾ of the (HPO$_3$)$^{2-}$ are located on walls of the larger hexagonal channels.[1-3]
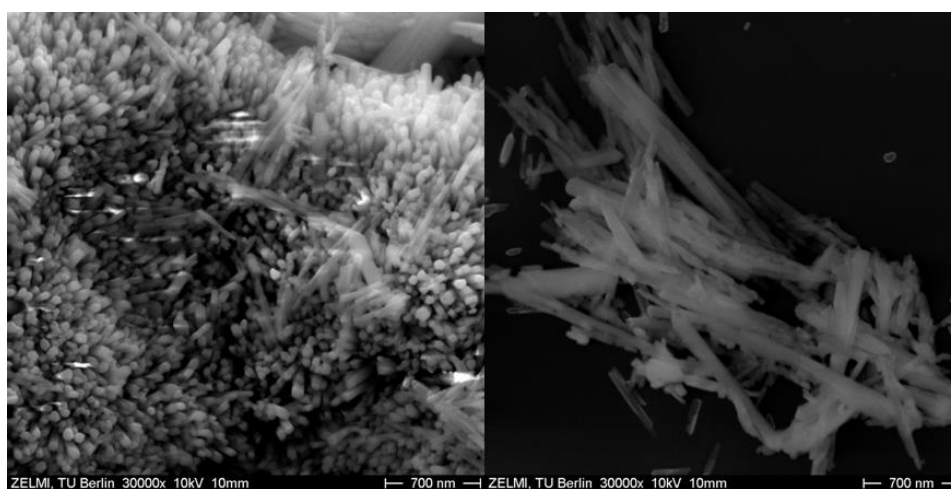

Figure S3. SEM micrographs of as-prepared Ni$_{11}$(HPO$_3$)$_8$(OH)$_6$ displaying rod-morphology.

3

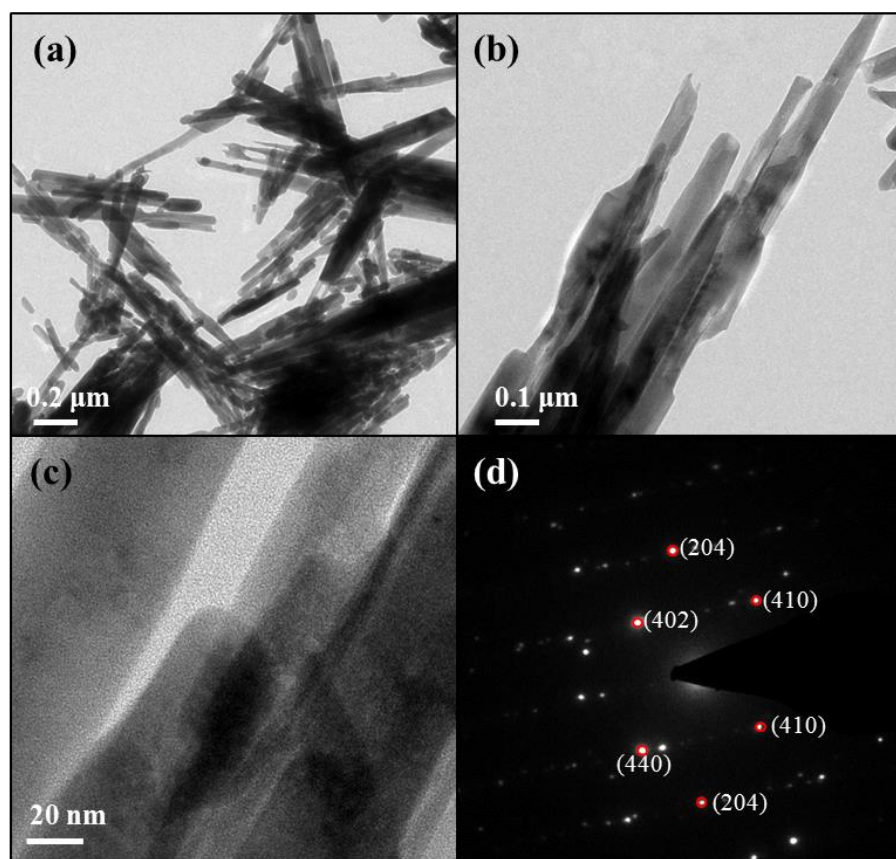**Figure S4**. TEM (a) and high-resolution TEM (b, c) images $Ni_{11}(HPO_3)_8(OH)_6$.[1] The reflection in selected area electron diffraction pattern (SAED) can be perfectly matched with the planes of nickel phosphite indicating the formation of a pure phase.
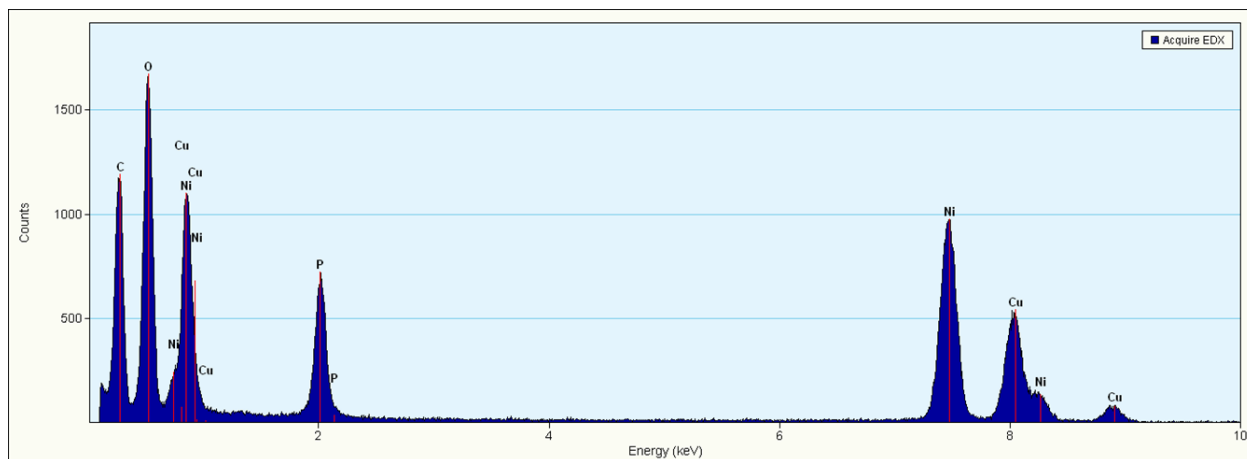
Figure S5. The presence of nickel and phosphorous in $Ni_{11}(HPO_3)_8(OH)_6$ was determined by the EDX measurements. Appearances of peaks for copper are due to TEM grid (carbon film on 300 mesh Cu-grid).
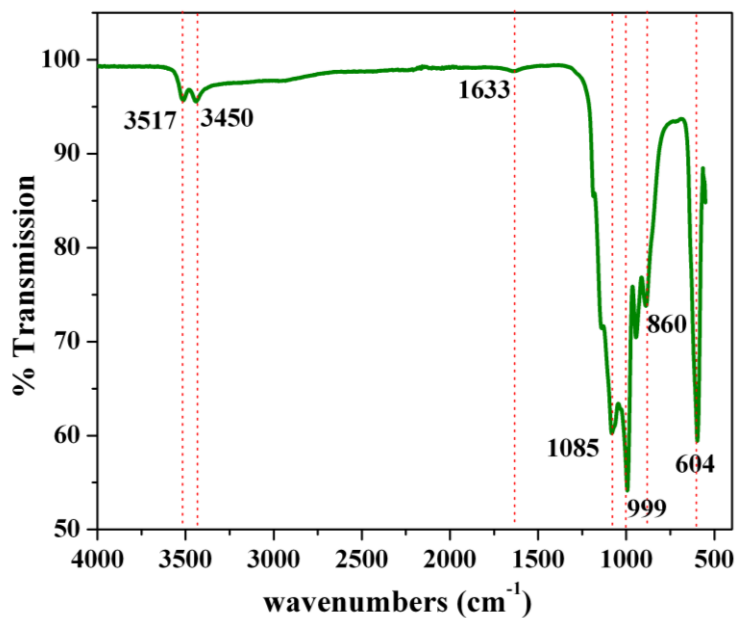

Figure S6. FT-IR transmission spectrum of as-prepared $Ni_{11}(HPO_3)_8(OH)_6$.[4] The broad band ranging from 3300 cm^{-1} to 3600 cm^{-1} and the bands at 1633 cm^{-1} are assigned to the O–H stretching vibration of the remaining water, exchangeable OH^-, and deficient OH groups with a large amount of hydrogen bonding respectively. The band at 1085 cm^{-1} are because of the deformation of terminal P–H and while the band at 1085 and 999 cm^{-1} is ascribed to P–O stretching vibrations confirming the presence of $(HPO_3)^{2-}$ moiety. Further, in the low wavenumber regions, the bands at 860 cm^{-1} could be corroborated with vibrations of H–P–O whereas the bands at 604 cm^{-1} are attributed to deformation of Ni–OH.[4]

Table S2. The distribution of the area in the region of Ni $2p_{3/2}$ and Ni $2p_{1/2}$ XPS with respect to the binding energy (BE) and various oxidation states and satellites for as-synthesized $Ni_{11}(HPO_3)_8(OH)_6$ and after OER CA experiments.

The Ni XPS spectra exhibited peaks at the binding energies of 855.8 and 873.6 eV for Ni^{2+} ($Ni(OH)_2$) whereas peaks at 857.6 and ~ 877 eV are attributed to the presence of Ni^{3+} in the structure (Fig. S26).[35,55] In addition, three satellite peaks, due to multi-electron excitation were also achieved that are characteristics of materials containing Ni (Fig. S26).[74] The resulting Ni^{2+} and Ni^{3+} percentage distribution in OER CA and HER CA along with their satellites in the area of Ni $2p_{3/2}$ and Ni $2p_{1/2}$ region is presented in Table S2. Notably, after OER CA, the amount of Ni^{2+} to Ni^{3+} was slightly higher than the as-prepared sample whereas no drastic changes were observed after HER CA. Interestingly, the surface atomic Ni:P composition of as-prepared, OER CA and HER CA was ~ 1:0.7, evidencing stability of nickel phosphite structures.

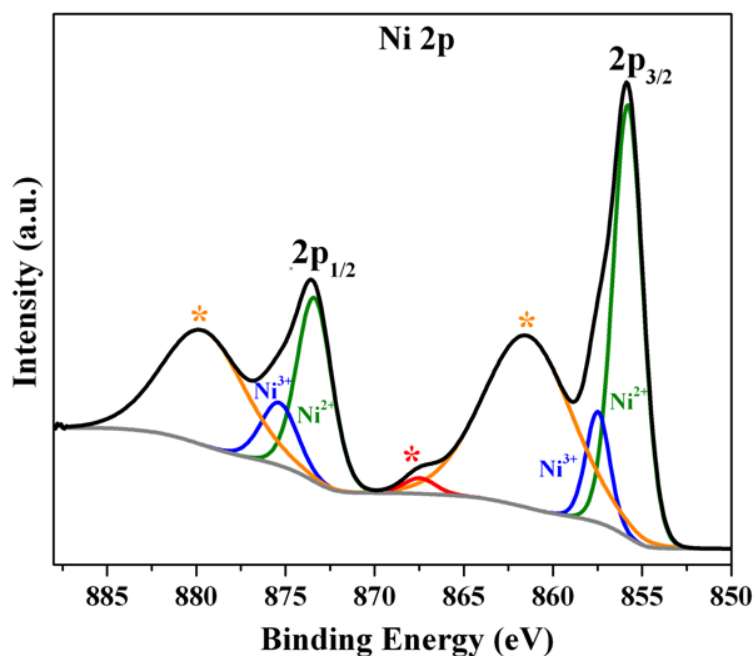|	BE in eV	As-synthesized area in %	OER CA area in %	HER CA area in %
Ni $2p_{3/2}$ (Ni^{2+})	~ 855.8	26.32	28.93	25.85
Ni $2p_{1/2}$ (Ni^{2+})	~ 873.4	12.97	14.25	12.73
Ni $2p_{3/2}$ (Ni^{3+})	~ 857.4	05.36	7.15	08.77
Ni $2p_{1/2}$ (Ni^{3+})	~ 875.3	04.60	12.67	06.83
Satellite 1	~ 861.4	30.87	28.20	26.96
Satellite 2	~ 867.4	01.01	00.76	02.35
Satellite 2	~ 880	18.87	08.84	16.50

Figure S7. The deconvoluted core-level Ni 2p XPS spectra of $Ni_{11}(HPO_3)_8(OH)_6$.[2,3] Both the deconvoluted regions of Ni $2p_{3/2}$ and Ni $2p_{1/2}$ exhibited one major and one minor peak. The major peak at the binding energy of 855.8 and 873.4 eV could be assigned to the Ni^{2+} ($Ni(OH)_2$) whereas the minor peak at 857.4 and 875.3 eV are attributed to the presence of a slight amount of Ni^{3+} in the structure.[5-9] In addition, three satellite peaks, due to multi-electron excitation were also observed within the deconvoluted regions of Ni $2p_{3/2}$ and Ni $2p_{1/2}$ at 861.4, 867.4 and 879.6 eV that are characteristics of materials containing Ni.[10,11] The resulting Ni^{2+} and Ni^{3+} percentage distribution along with their satellites in the area in the Ni $2p_{3/2}$ and Ni $2p_{1/2}$ region are presented in Table S2. Comparing the deconvoluted spectra with the other literature reported examples, it was evident that the overall oxidation state of Ni is nickel phosphite is somewhat higher than +2. The surface atomic Ni:P composition of-prepared material of was 1:0.70.
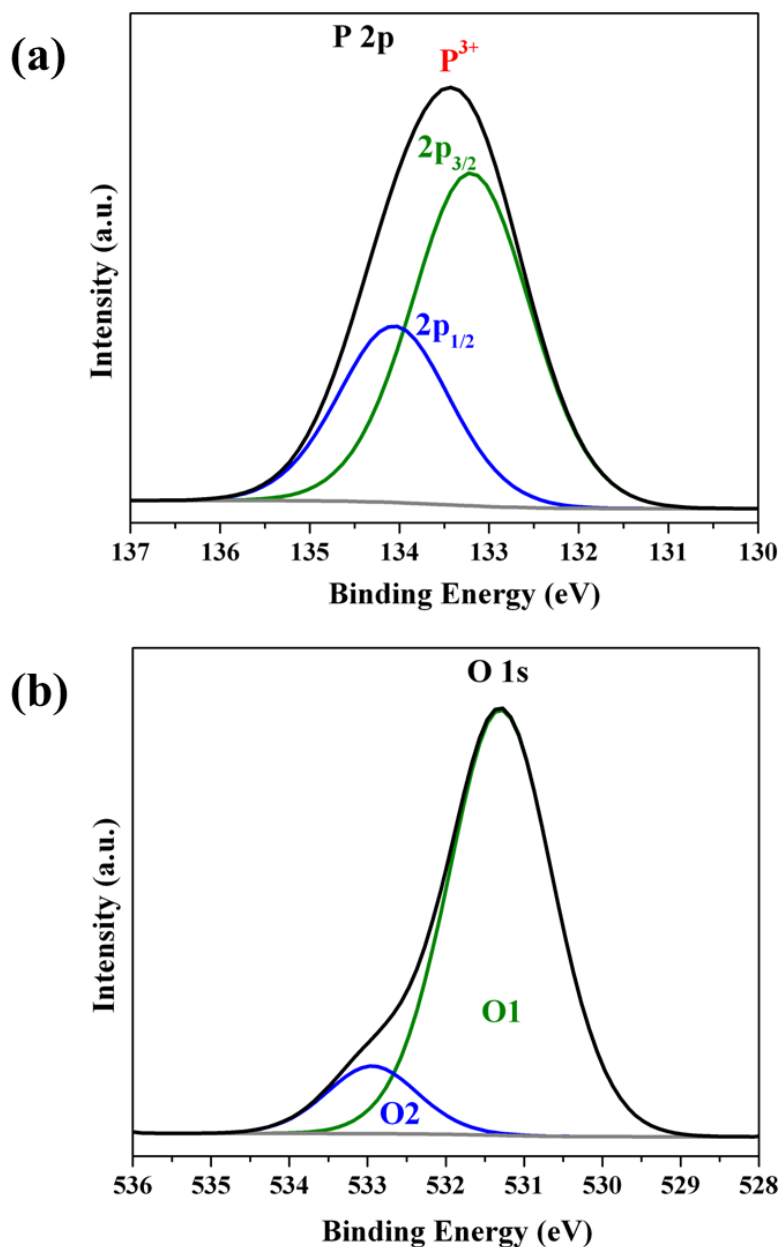
Figure S8. The core-level (a) P 2p and (b) O 1s XPS spectra of $Ni_{11}(HPO_3)_8(OH)_6$. The P 2p (a) spectrum displayed a broad peak at 133.5 eV.[2] The deconvoluted spectrum of P 2p showed two signals at 133.2 and 134 eV corresponding to P $2p_{3/2}$ and P $2p_{1/2}$. The obtained values here confirm that all P atoms are in the +3 oxidization state and in accordance with the metal phosphites in the literature.[2,3] The O1s spectrum (b) could be deconvoluted into O1 and O2 where the peak O1 at 531.3 eV is characteristic to oxygen (oxygen in the 2- oxidation state) in phosphites as well as hydroxyl groups.[2,3] The second peak O2 at 533 eV is associated with the bound water of hydration and are consistent with the known nickel phosphites as well nickel-containing hydroxide materials.[2,3,12]
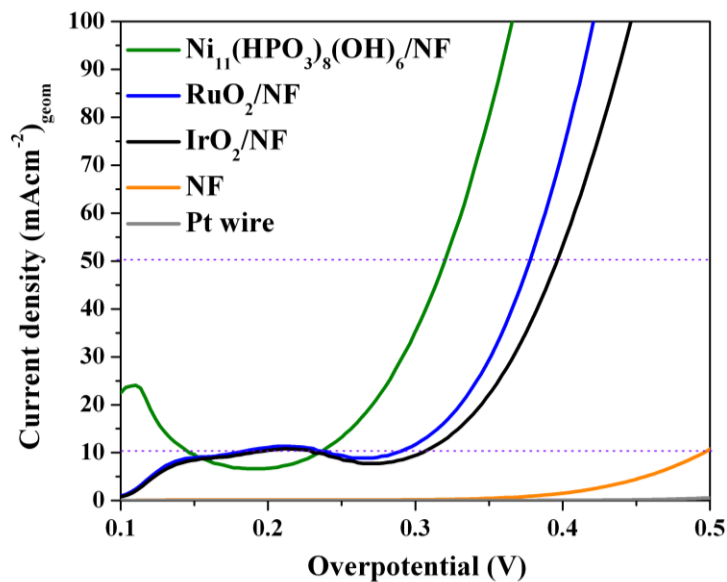
Figure S9. Comparison of overpotentials (at 10, 50 and 100 mAcm^{-1}) obtained from LSV's of remarkably active Ni$_{11}$(HPO$_3$)$_8$(OH)$_6$ and other non-noble based systems on NF in aqueous 1 M KOH with a sweep rate 1 mV/s. The acquired overpotentials are enlisted in Table S3.
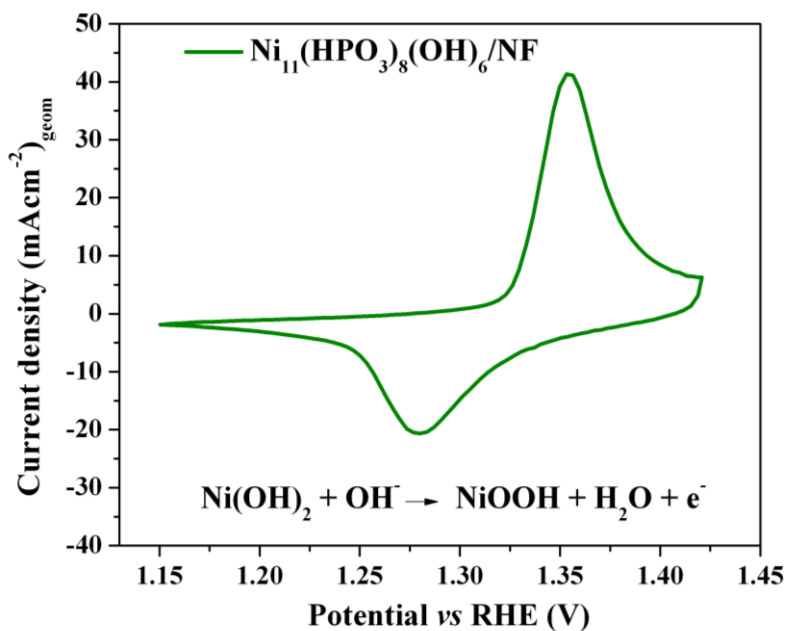

Figure S10. CV of Ni$_{11}$(HPO$_3$)$_8$(OH)$_6$ measured between 1.15 to 1.45 V (vs RHE) in 1 M KOH on NF with a sweep rate 1 mV/s featuring a pair of anodic and cathodic peaks corresponding to the reaction Ni(OH)$_2$ + OH$^-$ → NiOOH + H$_2$O + e$^-$. From the voltammogram, it was evident that Ni^{2+} reversibly converted into Ni^{3+} which also serves as a catalytically active site along with Ni^{2+} for the oxygen evolution.[13-16]
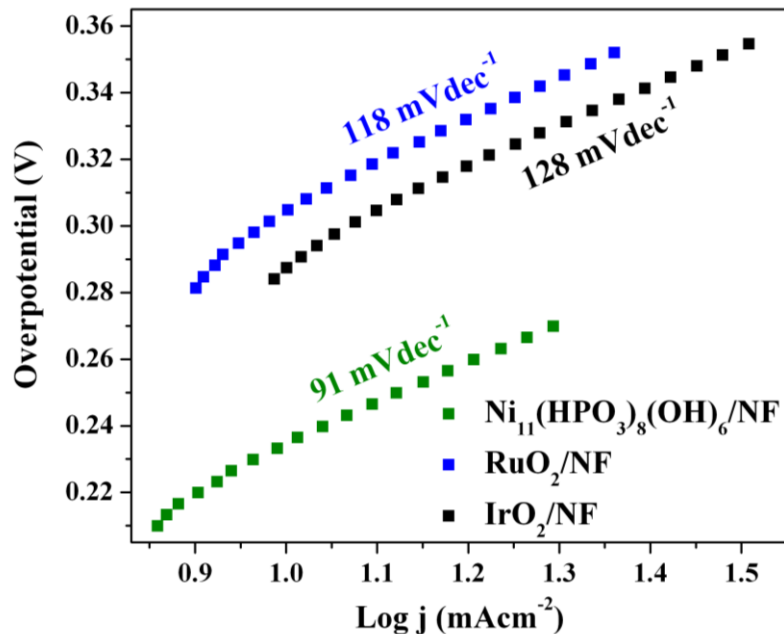
Figure S11. The Tafel plots of $Ni_{11}(HPO_3)_8(OH)_6$ and commercial RuO_2 and IrO_2 on NF in aqueous 1 M KOH solution in OER.
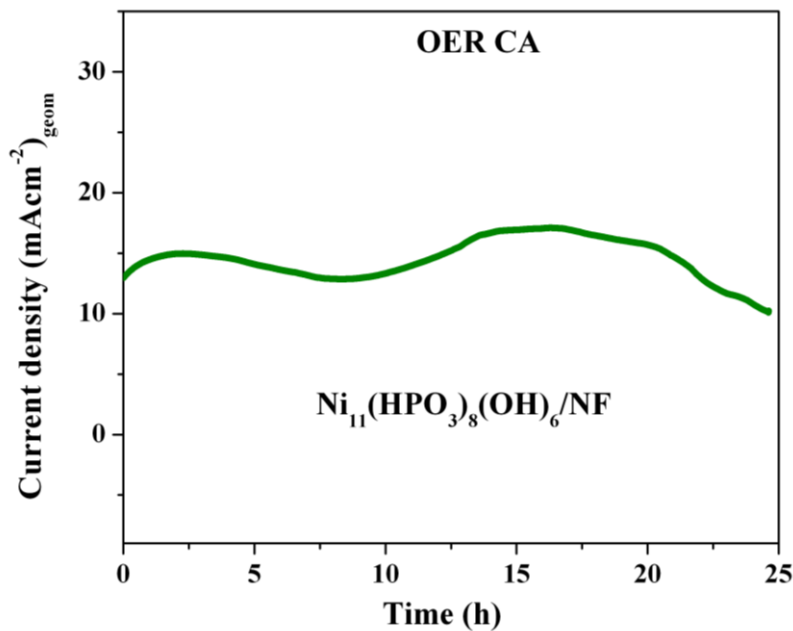

Figure S12. The CA responses of $Ni_{11}(HPO_3)_8(OH)_6$ on NF measured in OER conditions at an overpotential of 240 mV in 1 M KOH solution. The catalyst was very stable for more than 24 h. The minor decrease in current in the middle is attributed to the evaporation of the electrolyte and when a fresh solution of KOH was added from the top to fill the electrode level, an increase in current was observed.
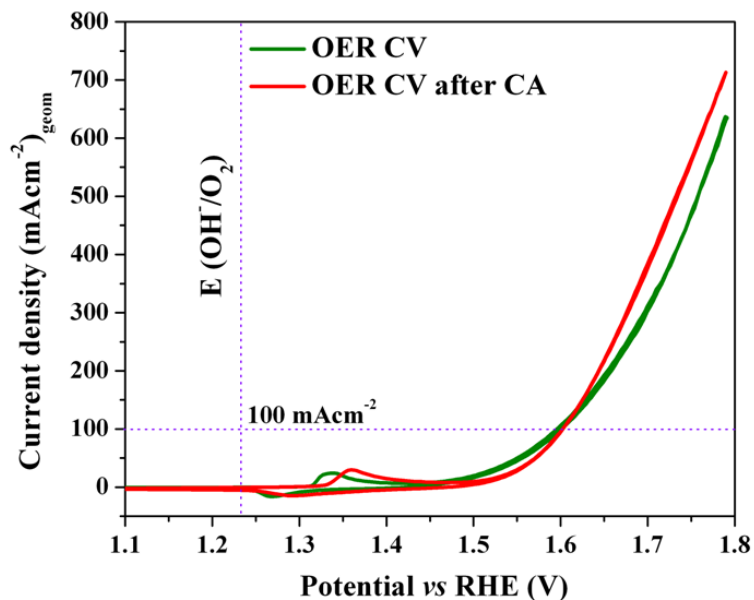
Figure S13. The initial CV of $Ni_{11}(HPO_3)_8(OH)_6$ and the CV measured after CA over the period 24 h in 1 M KOH on NF with a sweep rate 1 mV/s (vs RHE). Although a 20 mV decrease in overpotential at a current density of 10 mAcm^{-2} was attained after CA, however, in the higher current density region, better overpotentials resulted.

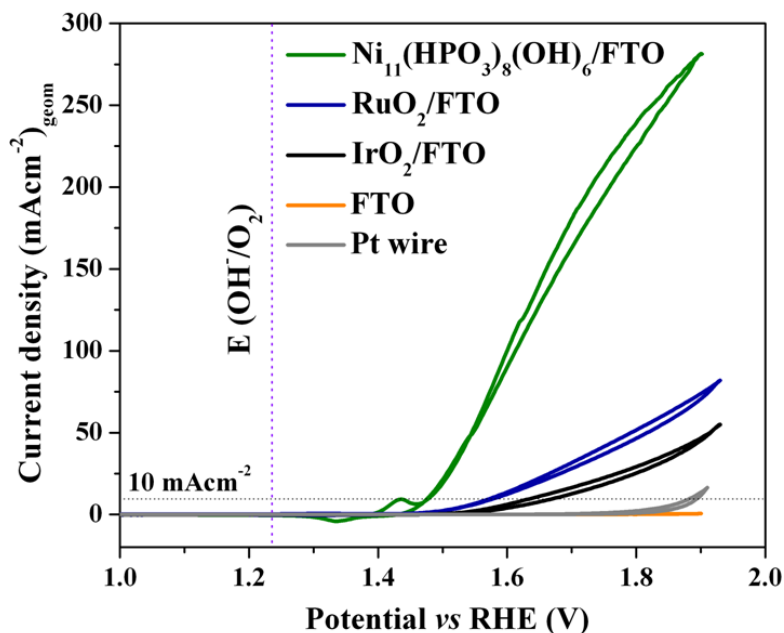**Figure S14**. CV's of $Ni_{11}(HPO_3)_8(OH)_6$ and noble metal based systems on FTO with a sweep rate 1 mV/s in 1 M KOH solution (vs RHE) for OER. The $Ni_{11}(HPO_3)_8(OH)_6$ was extremely active yielding an overpotential of merely 246 mV at 10 mAcm^{-2} compared to other catalysts. The overpotentials are listed in Table S3.

11
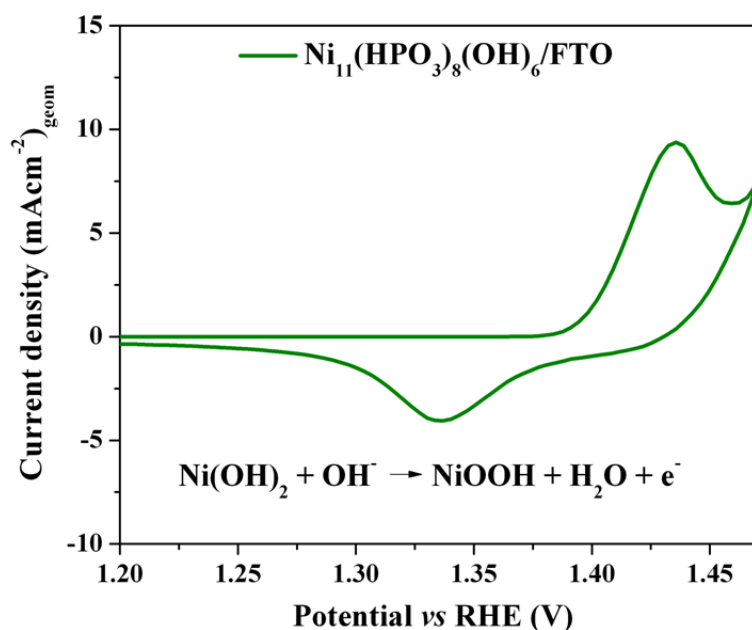
Figure S15. CV of $Ni_{11}(HPO_3)_8(OH)_6$ measured between 1.2 to 1.45 V (vs RHE) in 1 M KOH on FTO with a sweep rate 1 mV/s featuring a pair of anodic and cathodic peaks attributed to Ni^{2+}/Ni^{3+} similar to $Ni_{11}(HPO_3)_8(OH)_6$ on NF. This also rules out the possible contribution of NF in catalysis.[13-16]

Figure S16. The CA responses of $Ni_{11}(HPO_3)_8(OH)_6$ on FTO measured in OER conditions at an overpotential of 250 mV in 1 M KOH solution. The catalyst was stable for more than 24 h with only 10% decrease in the total current.

12

Table S3. The comparison of OER and HER overpotentials of $Ni_{11}(HPO_3)_8(OH)_6$ with other benchmark noble based catalysts on FTO and NF in 1M KOH solution.

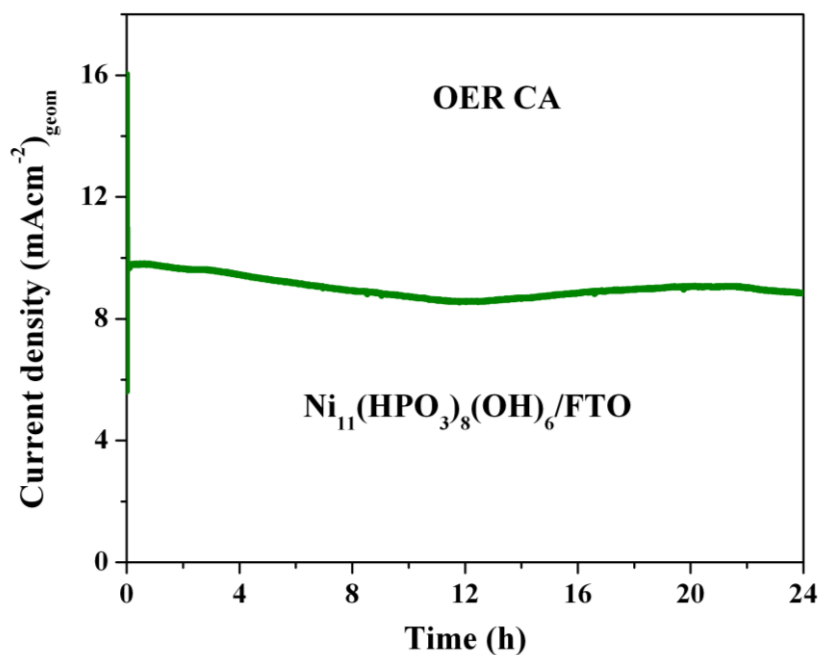| Catalyst	Current density $(mAcm^{-2)}$	OER overpotential (mV)	Current density $(mAcm^{-2)}$	HER overpotential (mV)
		On FTO		
$Ni_{11}(HPO_3)_8(OH)_6$	**10**	**246**	**-10**	**336**
IrO_2	10	400	-10	428
RuO_2	10	354	-10	-
Pt wire	10	-	-10	42
FTO	10	650	-10	-
		On NF		
$Ni_{11}(HPO_3)_8(OH)_6$	**10**	**232**	**-10**	**121**
	100	**364**	**-100**	**274**
Pt	10	-	-10	42
	100	-	-100	130
IrO_2	10	310	-10	211
	100	445	-100	335
RuO_2	10	292	-10	229
	100	420	-100	370
NF	10	490	-10	246
	100	-	-100	494
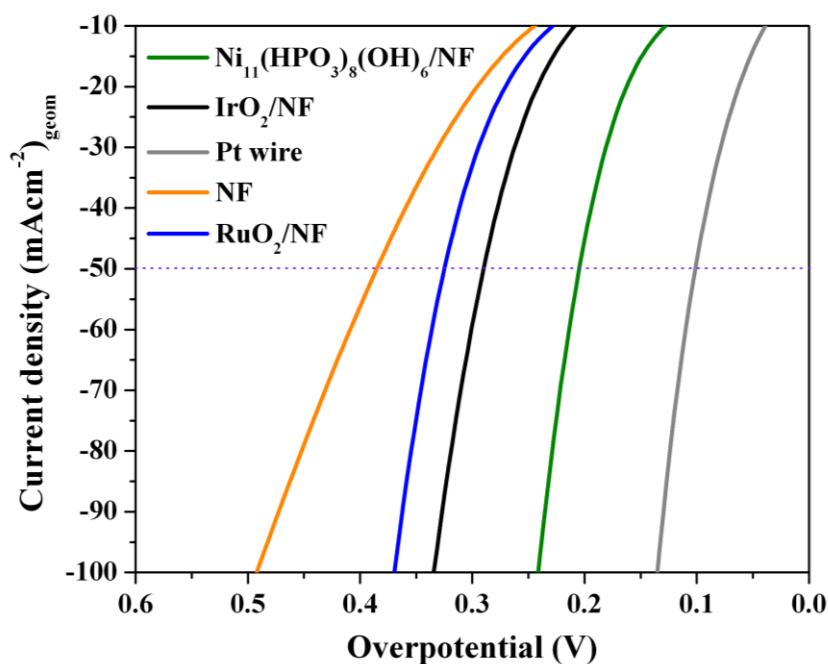
Figure S17. Comparison of overpotentials (at 10, 50 and 100 mAcm^{-2}) obtained from LSV's (HER) of Ni$_{11}$(HPO$_3$)$_8$(OH)$_6$ and other noble based systems on NF in 1 M KOH with a sweep rate 5 mV/s. The acquired overpotentials are enlisted in Table S4.
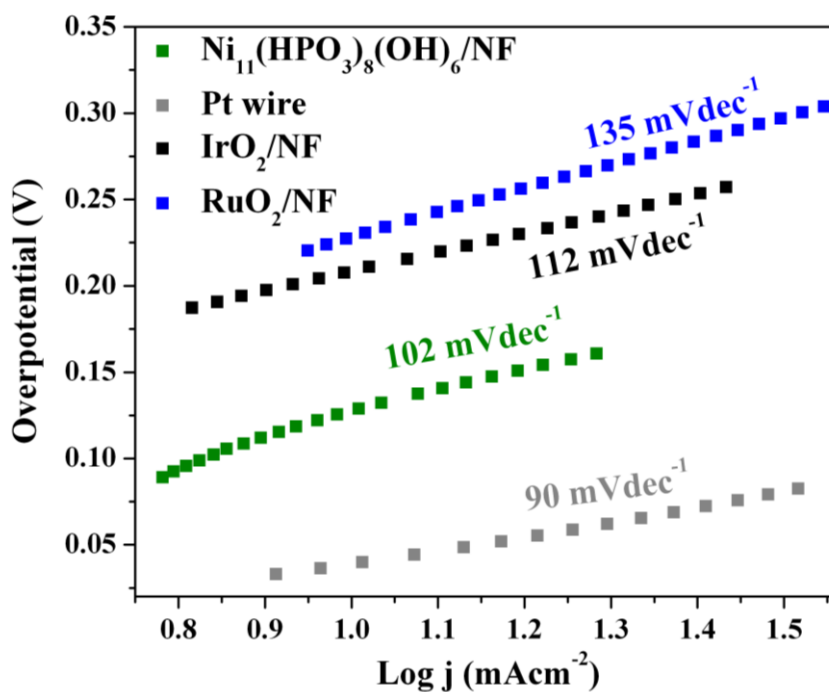
Figure S18. The Tafel plots of Pt wire, Ni$_{11}$(HPO$_3$)$_8$(OH)$_6$ and commercial RuO$_2$ and IrO$_2$ on NF in aqueous 1 M KOH solution in HER.

14

Figure S19. The CA responses of $Ni_{11}(HPO_3)_8(OH)_6$ on NF measured in OER conditions at an overpotential of 130 mV in 1 M KOH solution. The catalyst was stable with only 10% decrease when tested for more than 24 h.
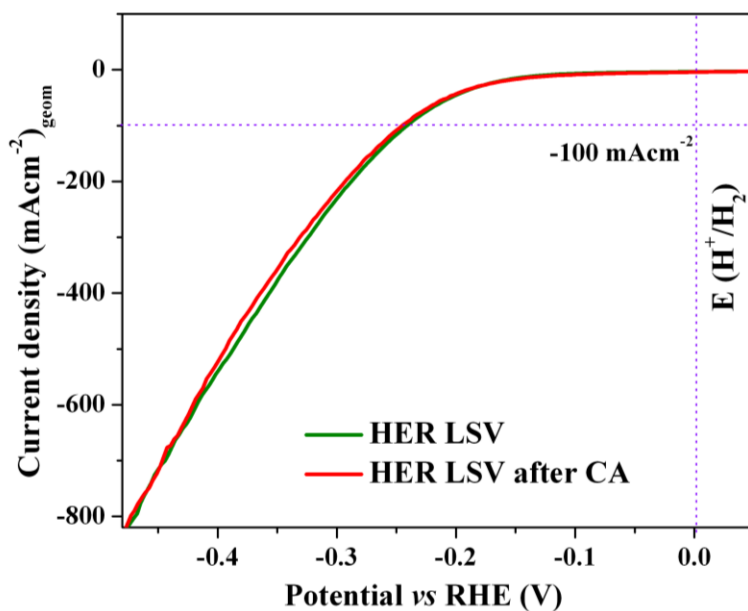
Figure S20. The initial LSV of $Ni_{11}(HPO_3)_8(OH)_6$ and the LSV measured after CA (over 24 h) in 1 M KOH on NF with a sweep rate 5 mV/s (vs RHE) for HER. Almost no change in the overpotentials was attained demonstrating the excellent stability of the catalyst.

15
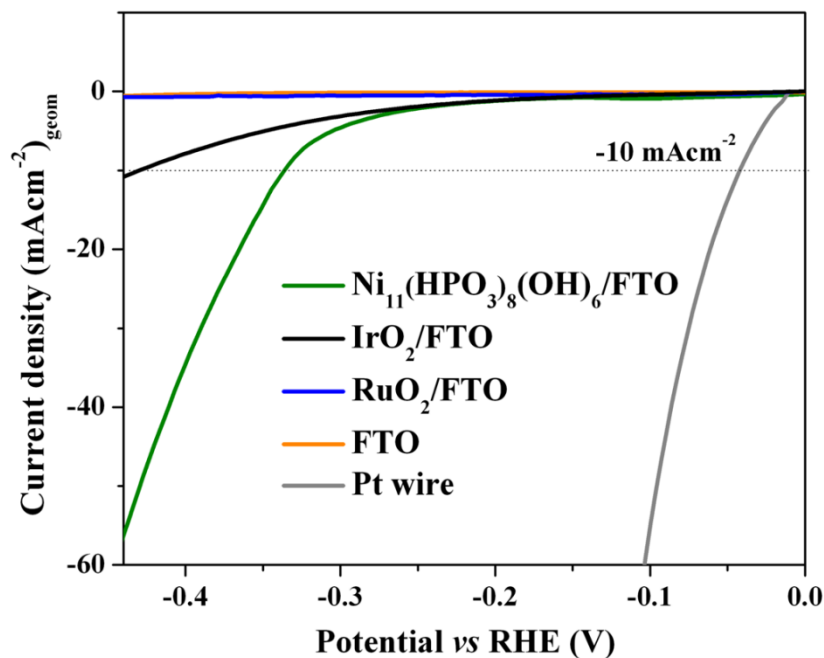
Figure S21. LSV's of $Ni_{11}(HPO_3)_8(OH)_6$ and other noble based systems on FTO with a sweep rate 5 mV/s in 1 M KOH solution (vs RHE). The $Ni_{11}(HPO_3)_8(OH)_6$ was moderately active for HER. The overpotentials are listed in Table S4.
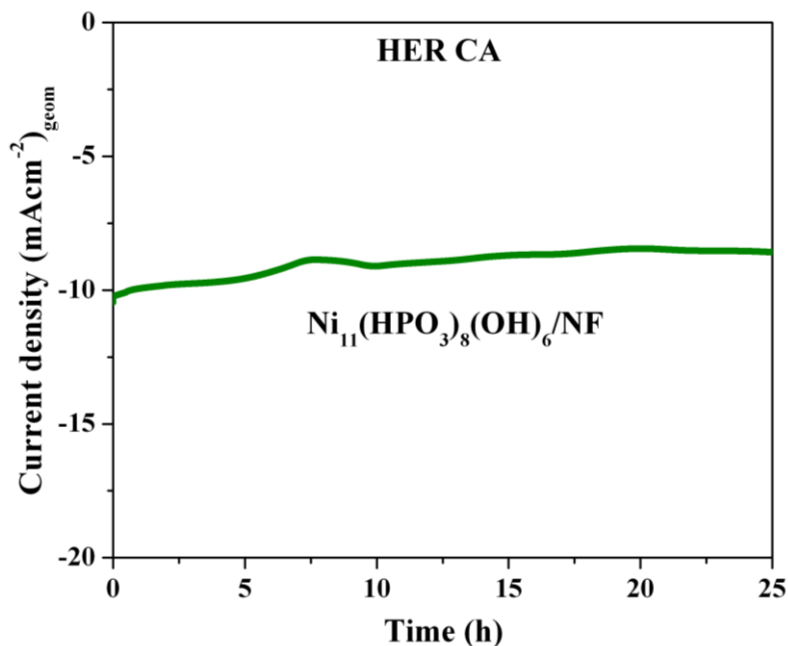

Figure S22. The CA responses of $Ni_{11}(HPO_3)_8(OH)_6$ on FTO measured in HER conditions at an overpotential of 330 mV in 1 M KOH solution. The catalyst slightly (20%) loses its activity when tested for more than 24 h (due to the slow evopration of electrolyte).

16

Table S4. The comparison of OER overpotentials of $Ni_{11}(HPO_3)_8(OH)_6$ with other superior selected non-noble catalysts 1 M KOH (pH 14).

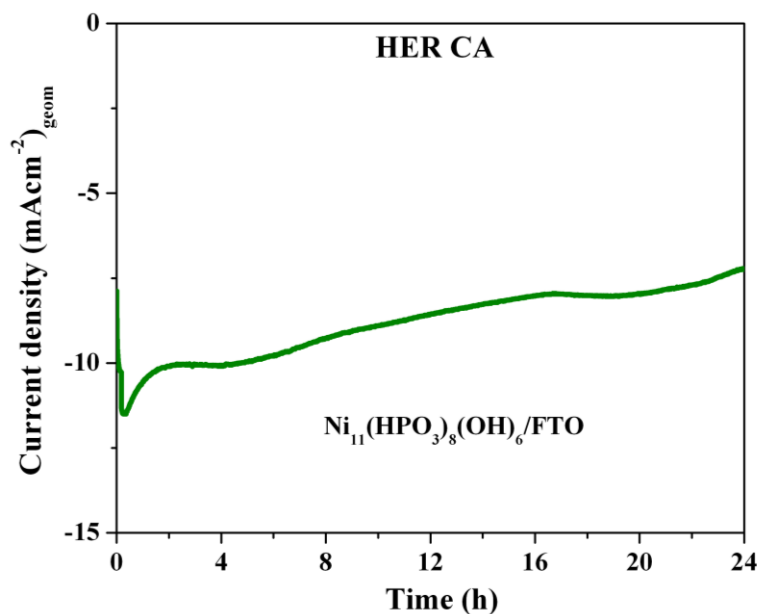| Catalyst	Current density ($mAcm^{-2}$)	Overpotential (mV)	Reference
$Ni_{11}(HPO_3)_8(OH)_6$ /NF	**10**	**232**	**This work**
	100	**364**	**This work**
$Ni_{11}(HPO_3)_8(OH)_6$ /FTO	**10**	**246**	**This work**
$Fe(PO_3)_2/Ni_2P/NF$	10	177	[17]
CoO_x@CN	10	260	[18]
Ni_2P/NF	10	240	[16]
$Ni_{12}P_5$/NF	10	260	[16]
MoO_2/NF	10	250	[19]
NiFe LDH	10	260	[20]
$Ni(OH)_2$/NF	10	330	[21]
Ni-P	10	300	[22]
NiCo-MOF	10	250	[23]
NiFe-MOF	10	240	[24]
Ni_2P/FTO	10	400	[25]
Ni_2P/FTO	10	500	[25]
Ni_2P/Ni/NF	10	200	[26]
Ni_xP_y-325	10	320	[27]
Ni_2P/GC	10	290	[28]
Ni_5P_4 films	10	290	[29]
Ni-P film	10	344	[30]
Co-P/Cu	10	345	[31]
NiCo/NS	10	334	[32]
NiCo LDH	10	367	[33]
$Ni_xCo_{3-x}O_4$ NWs/Ti	10	370	[34]
Ni_3S_2/NF	10	250	[35]
NiSe/NF	10	215	[36]
$Ni_{1-x}Fe_x$ NC/GC	10	330	[37]
Co_3O_4/ $NiCo_2O_4$ DSNCs	10	340	[38]
CoP/Cu	10	345	[30]
CoCo LDH	10	393	[32]
CoO_x/CN	10	260	[18]
$FeOOH/CeO_2$/NF	10	250	[39]
N-G/CoO	10	340	[40]
Co_3O_4/N-rmGO	10	310	[41]
$CoFeO_x$	10	360	[42]
$NiFeO_x$	10	350	[42]
Co_3O_4@CoP	10	238	[43]
MoO_2/NF	10	250	[19]
MoO_2/NF compact	10	500	[19]
FeP/Au	10	290	[44]
FeP RGO/Au	10	260	[44]

Table S5. The comparison of HER overpotentials of $Ni_{11}(HPO_3)_8(OH)_6$ with other highly active selected non-noble catalysts in 1 M KOH (pH 14).

Catalyst	Current density ($mAcm^{-2}$)	Overpotential (mV)	Reference
$Ni_{11}(HPO_3)_8(OH)_6$ /NF	**-10**	**121**	**This work**
	-100	**271**	**This work**
$Ni_{11}(HPO_3)_8(OH)_6$ /FTO	**-10**	**336**	**This work**
MoS_2	-10	60	[45]
MoC	-10	77	[46]
MoB	-10	225	[47]
CoS_2	-10	175	[48]
CoMo	-10	170	[49]
CoS_2	-10	145	[50]
CoN_x	-10	140	[51]
Mo_2C	-10	130	[52]
Ni-NS	-10	80	[53]
$Ni(OH)_2$/NF	-10	172	[21]
Ni/Mo_2C-PC	-10	179	[54]
$Mo_{1-x}W_xS_2@Ni_3S_2$	-10	98	[55]
MoP/Ni_2P/NF	-10	75	[56]
$Co(S_xSe_{1-x})_2$	-10	130	[57]
Ni_2P	-10	87	[58]
Ni_2P/NF	-10	85	[16]
$Ni_{12}P_5$/NF	-10	170	[16]
Ni-P electrodeposited	-10	93	[30]
Ni_2P/GC	-10	220	[28]
Ni_xP_y-325	-20	160	[27]
Ni_2P/GEC	-20	205	[59]
NiFe LDH/NF	-10	200	[60]
Ni-NiO	-10	250	[61]
Ni_2P/GC	-20	250	[62]
Ni_5P_4 film	-10	180	[29]
$NiCo_2S_4$	-20	194	[63]
Ni_3S_2/NF	-10	220	[35]
Ni NC/GC	-10	219	[37]
CoO_x/CN	-10	232	[18]
CoO_x/CN	-20	352	[18]
CoNR CNT	-10	370	[64]
CoMn-S@NiO/CC	-100	232	[27]
CoP nanowire	-20	335	[65]
CoNiP/NF	-10	155	[25]
CoP/Cu	-10	94	[31]
CoP/CC	-10	209	[65]
MoC_x/C	-20	189	[66]

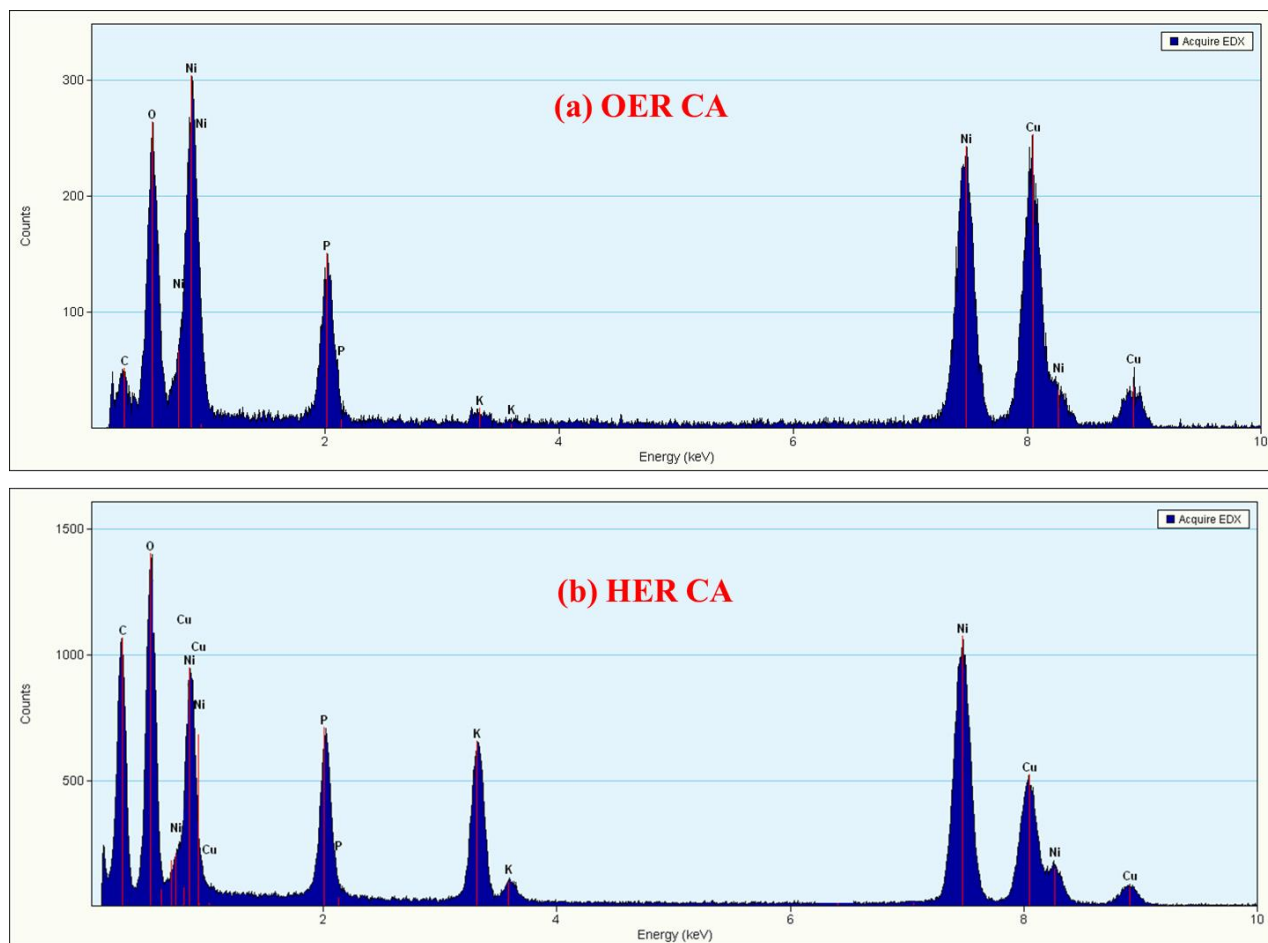**Figure S23**. Both in the case of (a), OER CA and (b) HER, the presence of nickel and phosphorous in $Ni_{11}(HPO_3)_8(OH)_6$ was determined by the EDX measurements. Appearances of peaks for copper are due to TEM grid (carbon film on 300 mesh Cu-grid) and a slight amount of potassium is from the electrolyte.
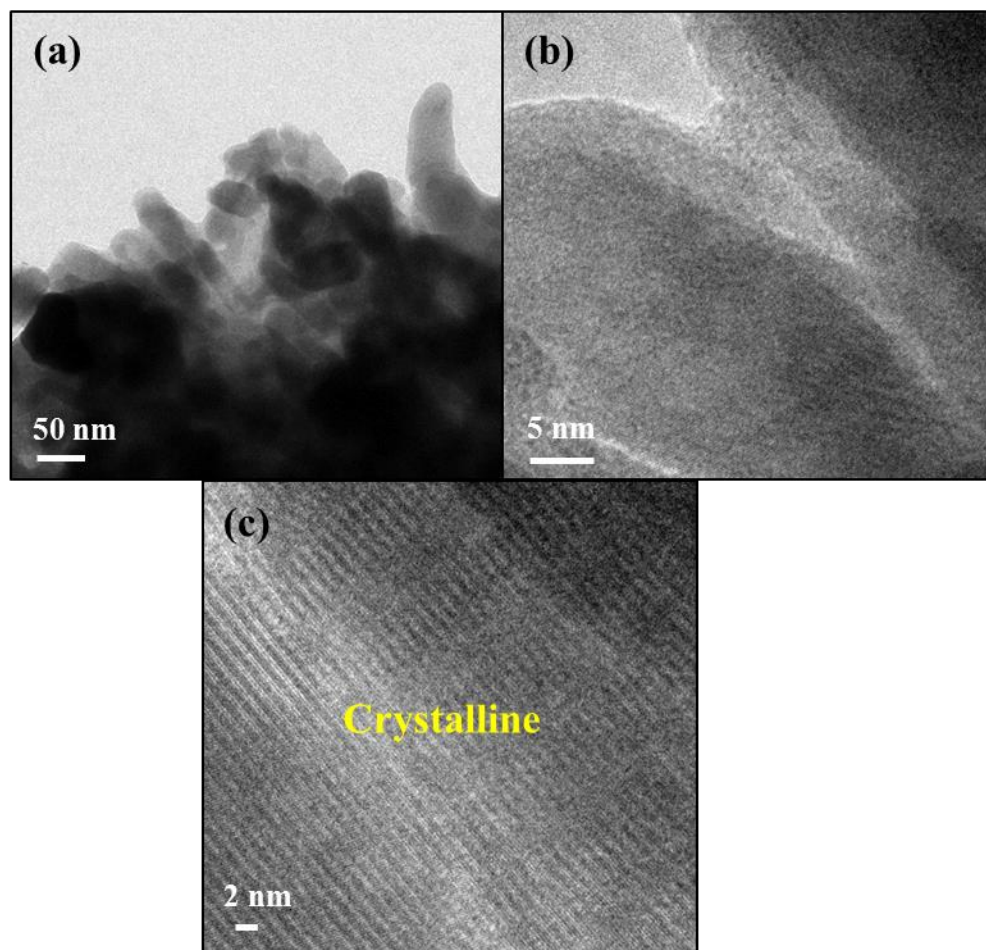
Figure S24. (a) TEM and (b, c) HR-TEM images of $Ni_{11}(HPO_3)_8(OH)_6$ after the OER CA measurements in aqueous 1 M KOH solution for 24 h. The HR-TEM image (b, c) showed crystalline particles without formation of any visible amorphous shell that confirmed pronounced stability and sustainability of the catalysts in the strongly alkaline medium unlike other transition metal-based reported examples in which often a thick amorphous layer and the intense structural changes at the surface are often unavoidable.

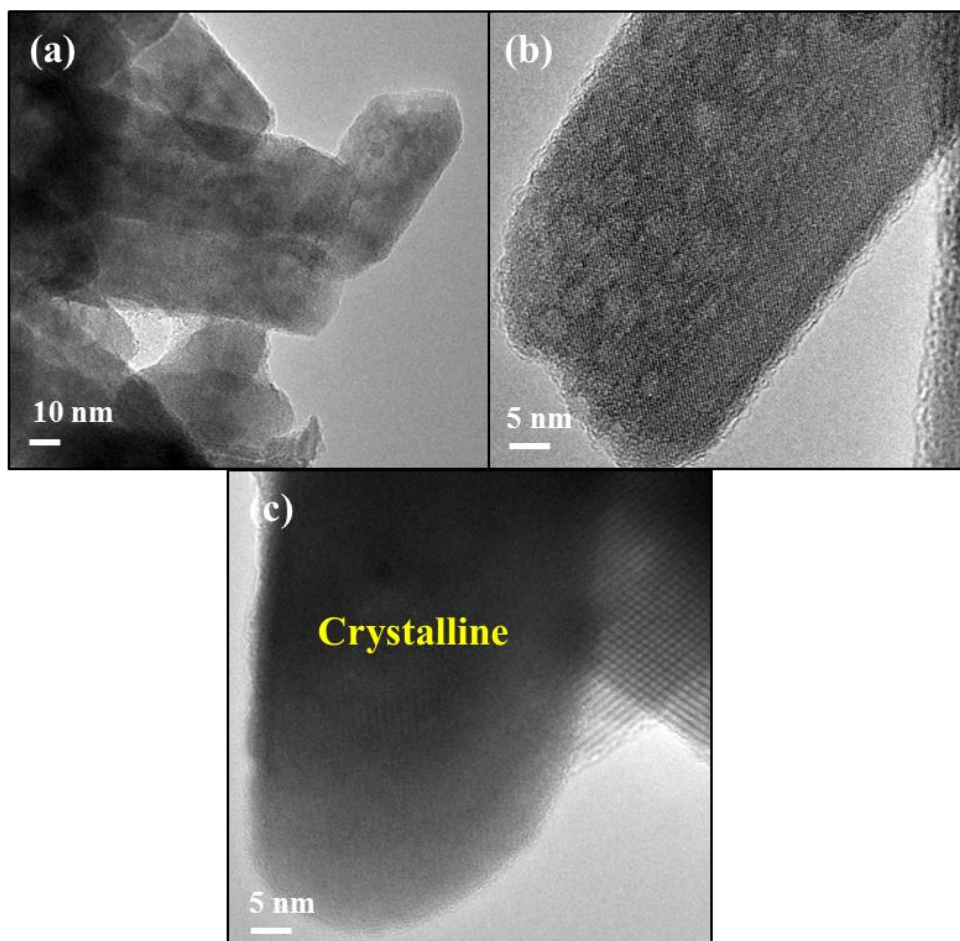**Figure S25.** (a) TEM and (b, c) HR-TEM images of $Ni_{11}(HPO_3)_8(OH)_6$ after the HER CA measurements in aqueous 1 M KOH solution for 24 h. From the HR-TEM images (b, c), it can be deduced that each particle was still crystalline (with crystalline borders) even after the strong alkaline HER conditions and did not undergo any phase transformation.
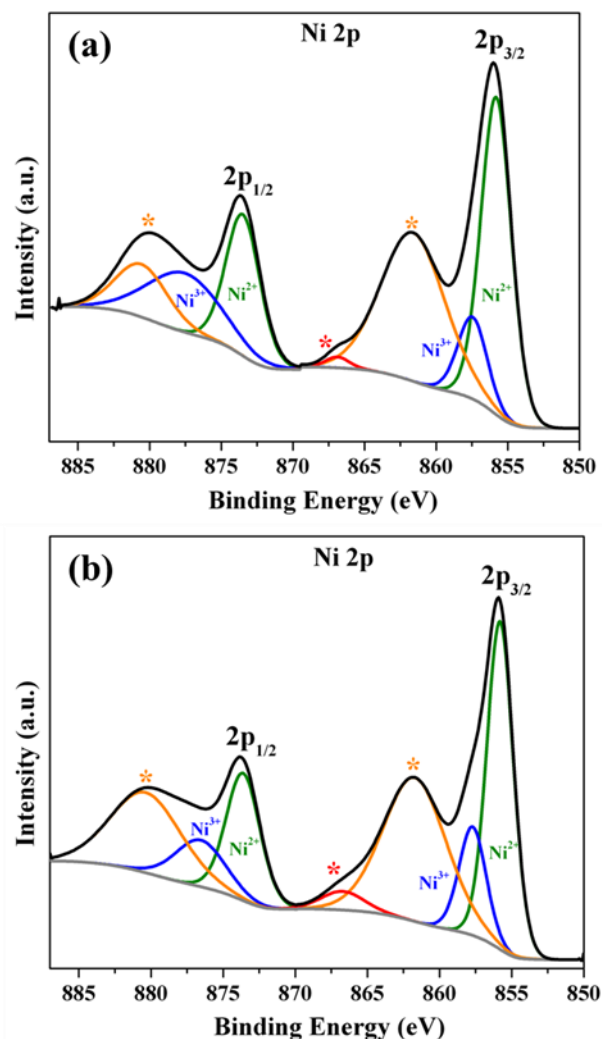
Figure S26. The deconvoluted core-level Ni 2p XPS spectra of $Ni_{11}(HPO_3)_8(OH)_6$ after (a) OER CA and (b) HER CA. Similar to the as-synthesized phosphite, the deconvoluted regions of Ni $2p_{3/2}$ and Ni $2p_{1/2}$ exhibited one major and one minor peak. In both cases, major peaks at the binding energies of 855.8 and 873.6 eV were assigned to Ni^{2+} ($Ni(OH)_2$) whereas minor peaks at 857.6 and ~ 877 eV could be attributed to the presence of a slight amount of Ni^{3+} in the structure.[5,8,9,11,67] In addition, three satellite peaks, due to multi electron excitation were also achieved within the deconvoluted regions of Ni $2p_{3/2}$ and Ni $2p_{1/2}$ at 861.8, ~ 867.2 and ~ 880 eV that are characteristics of materials containing Ni.[7,10] The resulting Ni^{2+} and Ni^{3+} percentage distribution in OER CA and HER CA along with their satellites in the area in the Ni $2p_{3/2}$ and Ni $2p_{1/2}$ region is presented in Table S2. Strikingly, after OER CA, the amount of Ni^{2+} to Ni^{3+} was slightly higher than the as-prepared sample whereas no drastic changes were observed after HER CA. This certainly evidences the superior stability of nickel phosphites towards surface corrosion. Interestingly, the surface atomic Ni:P composition of as-prepared, OER CA and HER CA was ~ 1:0.70.
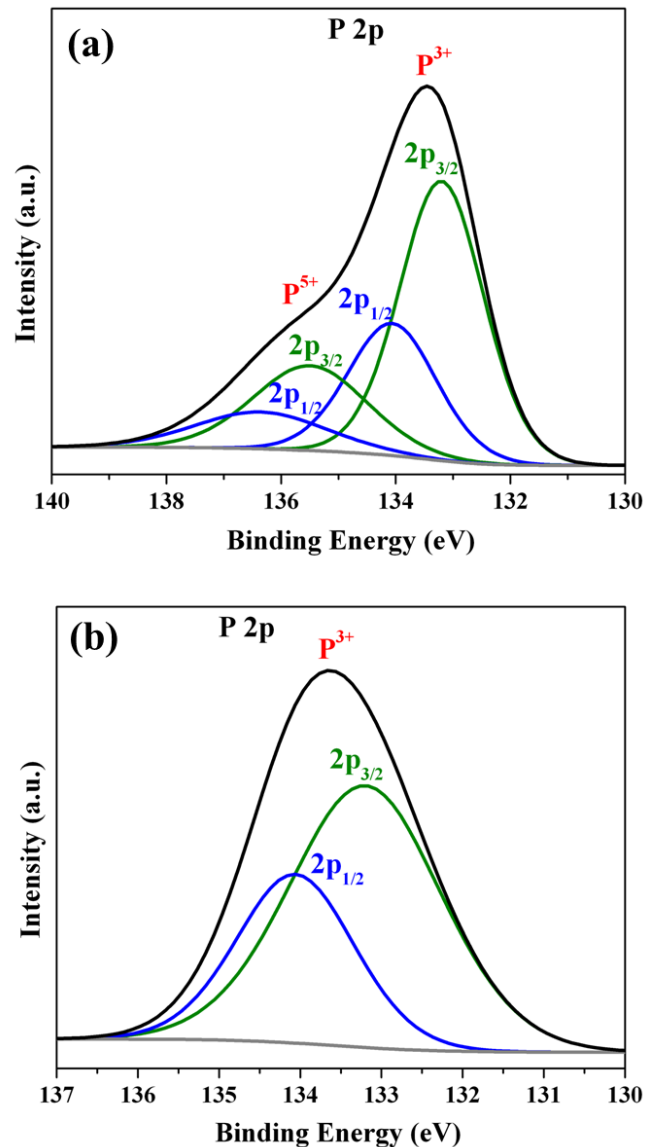
Figure S27. The detailed deconvolution of (a) OER CA and (b) HER CA. In the deconvolution spectra of (a) OER CA, the broad P 2p peak can be deconvoluted into four peaks, two corresponding to P $2p_{3/2}$ and P $2p_{1/2}$ at 133.2 and 134 eV for P^{3+} and other two at 135.4 and 136.3 eV for P^{5+}.[2,3,68] This shows that during OER CA, a tiny amount of P undergo oxidation forming phosphorous pentoxide on the surface.[68] However, in the case of (c) HER CA, two signals at 133.2 and 134 eV corresponding to P $2p_{3/2}$ and P $2p_{1/2}$ were acquired which is just similar to that of as-synthesized nickel phosphite revealing no further oxidation of phosphorus on the surface of the material. The obtained values here are well in the range of +3 and +5 oxidization state of P and in accordance with the metal phosphites as well P_2O_5 in the literature.[68,69]
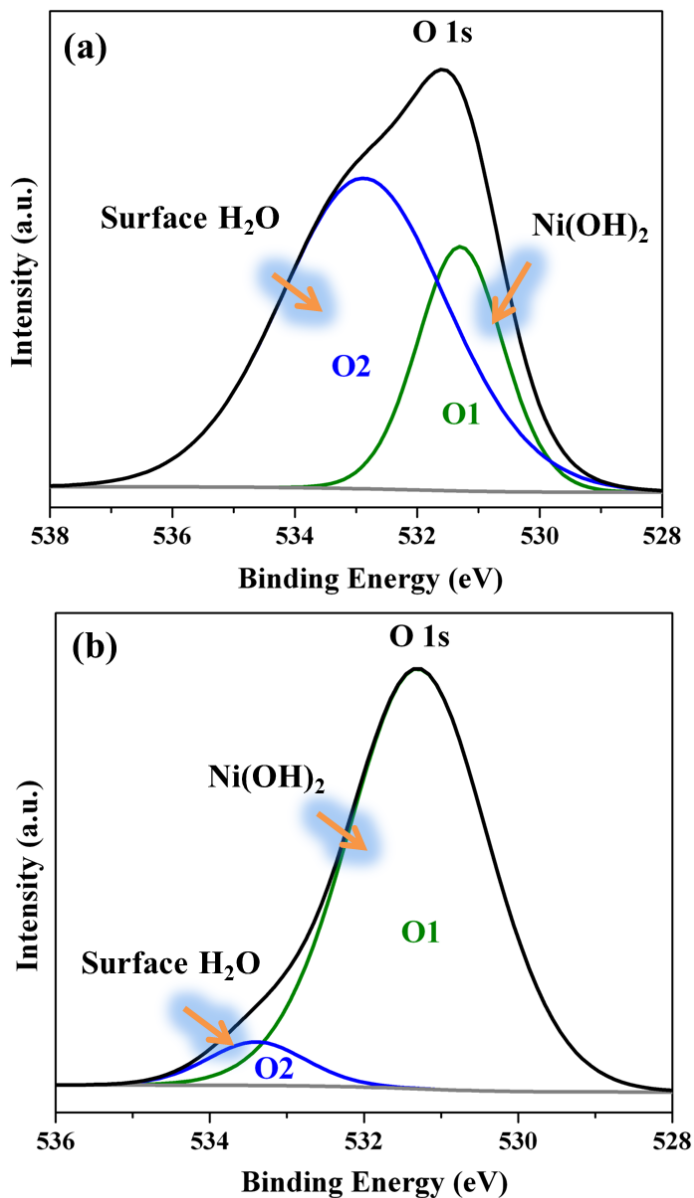
Figure S28. The deconvoluted O 1s XPS spectra of $Ni_{11}(HPO_3)_8(OH)_6$ materials of (a) after OER CA and (b) HER CA. In both cases, the spectra were deconvoluted into two peaks O1 and O2. The peak O1 at 531.3 eV is characteristic to oxygen (oxygen in the oxidation state of 2+) in phosphites as well as hydroxyl groups present in the structure.[2,3] The second peak O2 at 533 eV is associated with the bound water of hydration and is consistent with reported examples in the literature.[12,15,16] Strikingly, O 1s spectra of OER CA shows a large amount of bound water of hydration along with structural hydroxide demonstrating possible changes on the surface as observed in the case of HR-TEM. However, negligible difference in the O 1s spectra of HER CA was found while comparing with the as-prepared nickel phosphite material elucidating the stability of the surface species.

Table S6. Edge position and corresponding oxidation states deduced from the edge position of the Ni-K-edge (step-integral method reported by Dau et al, Anal. Bioanal. Chem. 2003, 376, 562-583) and from EXAFS simulations (bond valence sum).

compound	edge position/eV	oxidation state	oxidation state from bond valence sum (EXAFS simulation)
Ni-phosphite as prep.	8343.1	2.1	2.23
Ni-phosphite after OER CA	8343.1	2.1	2.24
Ni-phosphite after HER CA	8343.1	2.1	2.25

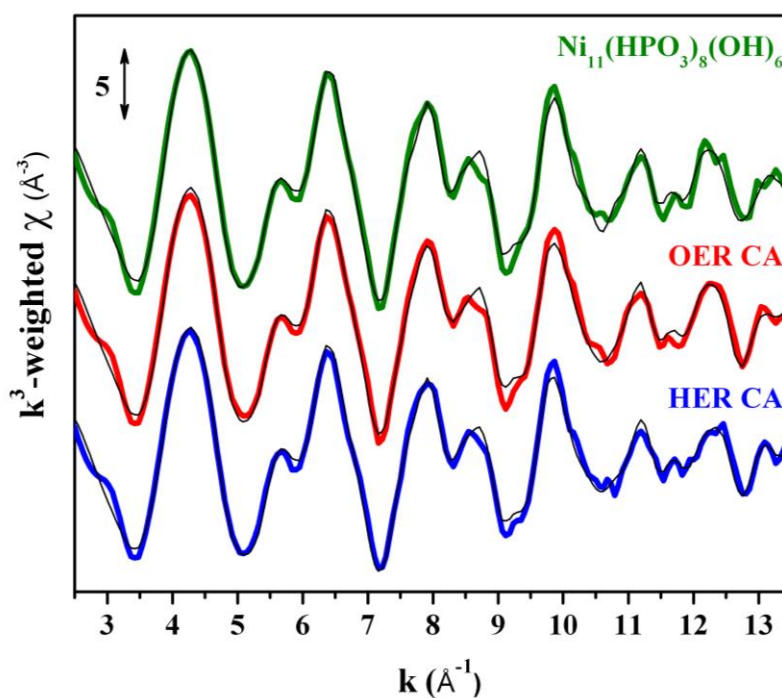**Figure S29.** k^3-weighted χ of experimental Ni EXAFS spectra of as-prepared $Ni_{11}(HPO_3)_8(OH)_6$, after OER CA and HER CA. The simulation parameters are given in Table S7. Thin black lines represent the simulation of the experimental data.

Table S7. Parameters obtained by the simulation (curve-fitting) of k^3-weighted EXAFS spectra of as-deposited $Ni_{11}(HPO_3)_8(OH)_6$ and after OER CA and HER CA for 24 h (N, coordination number; R, absorber-backscatter distance; σ, Debye-Waller parameter). Debye-Waller parameters for long-distance shells were fixed to reasonable values. Only single-scattering paths were included. The amplitude-reduction factor $S0^2$ was fixed to 0.75 as suggested by the simulation. Fitting was performed using in-house software (SimXLite) after calculation of the phase functions with the FEFF program (version 8.4, self-consistent field option activated). The phase functions have been calculated using a fragment of the crystal strucuture of $Ni_{11}(HPO_3)_8(OH)_6$ including 119 atoms (30 nickel atoms, 74 oxygen atoms and 15 phosphorous atoms). The error ranges of the fit parameters were estimated from the covariance matrix of the fit and represent the 68% confidence intervals (error calculations as described in reference[70-75]). The asterisks indicate parameters that were forced to the values given. For the Ni-O shells, the sum of the coordination number was fixed to be six. Cosine windows covering 10 % of the low k-side and 10 % of the high k-side of the spectra were applied before calculation of the Fourier transforms.

$Ni_{11}(HPO_3)_8(OH)_6$

shell	Ni-O	Ni-O	Ni-Ni	Ni-Ni	Ni-P	Ni-Ni	Ni-Ni	Ni-O	Ni-Ni	Ni-Ni	Ni-Ni	Ni-Ni	Ni-Ni
R [Å]	1.97	2.09	2.75	2.94	3.19	3.45	4.05	4.51	4.97	5.55	5.69	6.90	8.02*
error	0.01	0.01	0.01	0.01	0.01	0.02	0.01	0.01	0.02	0.01	0.02	0.01	-
σ [Å]	0.0447*	=s1	0.0671*	=s3	0.0592*	=s3	=s3	=s1	=s3	=s3	=s3	=s3	=s3
N	2.8	3.2*	1.2	1.9	3.0	0.5	1.2	3.0	1.1	4.0	2.8	3.9	5*
error	0.2	--	0.2	0.4	0.4	0.2	0.2	0.7	0.3	0.8	0.9	0.9	-
R-factor filtered (8.1 Å): 14.38													

$Ni_{11}(HPO_3)_8(OH)_6$ - OER CA

shell	Ni-O	Ni-O	Ni-Ni	Ni-Ni	Ni-P	Ni-Ni	Ni-Ni	Ni-O	Ni-Ni	Ni-Ni	Ni-Ni	Ni-Ni	Ni-Ni
R [Å]	1.97	2.09	2.75	2.94	3.18	3.45	4.05	4.50	4.98	5.55	5.70	6.90	8.0*
error	0.01	0.01	0.01	0.01	0.01	0.02	0.01	0.01	0.02	0.01	0.02	0.02	-
σ [Å]	0.0447*	=s1	0.0671*	=s3	0.0592*	=s3	=s3	=s1	=s3	=s3	=s3	=s3	=s3
N	2.7	3.3*	1.2	1.9	2.7	0.4	1.1	3.0	1.1	4.6	3.3	3.1	3*
error	0.1	--	0.2	0.4	0.4	0.2	0.2	0.7	0.4	0.8	0.9	0.9	-
R-factor filtered (8.1 Å): 13.36													

Ni$_{11}$(HPO$_3$)$_8$(OH)$_6$ - HER CA

shell	Ni-O	Ni-O	Ni-Ni	Ni-Ni	Ni-P	Ni-Ni	Ni-Ni	Ni-O	Ni-Ni	Ni-Ni	Ni-Ni	Ni-Ni	Ni-Ni
R [Å]	1.96	2.08	2.75	2.94	3.18	3.43	4.05	4.50	4.97	5.54	5.69	6.91	8.0*
error	0.01	0.01	0.01	0.01	0.01	0.01	0.01	0.02	0.01	0.01	0.01	0.01	-
σ [Å]	0.0447*	=s1	0.0671*	=s3	0.0592*	=s3	=s3	=s1	=s3	=s3	=s3	=s3	=s3
N	2.6	3.4*	1.1	1.8	2.4	0.7	1.1	2.4	1.4	5.2	4.3	3.6	3*
error	0.1	--	0.2	0.4	0.4	0.2	0.2	0.7	0.3	0.8	0.9	0.9	-
R-factor filtered (8.1 Å): 13.21													

Discussion of EXAFS simulations

The first peak in the FT (Fig. 6 and Fig. 7) represents Ni-O distances from Ni-O octahedral. The sum of oxygen ligands was forced to be six as suggested by the crystal structure of Ni$_{11}$(HPO$_3$)$_8$(OH)$_6$ where several Ni-O distances between 1.996 Å and 2.214 Å are present. Two oxygen shells were needed to simulate the experimental data appropriately (1.97 Å and 2.09 Å). The shorter Ni-O bond length is indicative of a Ni^{3+} contribution (likely Jahn-Teller-distortion) as it is a bit shorter than reported in the single crystal structure with Ni^{2+} only. This is in agreement with XPS data (Fig. S7). Peak number 2 and peak 3 (see Fig. 6 and Fig. 7) can be assigned to di-μ-oxo-bridged Ni atoms and Ni-P (peak 3) distances. Similarly to the reported bond lengths (2.68 Å, 2.98 Å and 3.13 Å for Ni-P), distances of 2.75 Å (Ni-Ni), 2.94 Å (Ni-Ni) and 3.18 Å (Ni-P) were observed. A high uncertainty for distances and coordination numbers is inevitable here due to the merging of Ni-Ni and Ni-P distances in the same peak (peak 3). Additionally, the mono-μ-oxo-bridged Ni-Ni distance connected via the phosphite group (Ni-OPO$_2$H−Ni) of 3.45 Å (3.51 Å reported) is close. A more accurate determination would include fitting of additional oxygen shells at ~ 3.5 Å interfering with the mono-μ-oxo-bridged Ni-Ni distance that has not been conducted in this study. Further, Ni-Ni shells can clearly be assigned to structural motifs within the Ni$_{11}$(HPO$_3$)$_8$(OH)$_6$ structure: mono-μ-hydroxo bridged Ni atoms within the (Ni$_4$O$_{12}$)$_n$ chain with a distance of 4.05 Å (4.01 Å in the crystal structure, peak number 7 in the FT). Along with this chain in (001) direction, a distance of 4.97 Å can be described by the connection of three Ni-O octahedra via each edge (peak 8). Peak number 2b at a distance of 4.50 Å most probably emerges as a result of oxygen shells (4.52 Å, 4.58 Å and 4.63 Å). A Ni-Ni distance of 5.61 Å (peak 10) in the crystalline compound resembles Ni-O$_6$ octahedra bound via the phosphite anion and were fitted with two distances (5.54 Å and 5.69 Å). This circumstance might reflect that protonated and deprotonated (H)PO$_3$ groups present at the same time. Peaks number 11 (~ 6.9 Å) and 12 (~ 8.0 Å) stem from longer Ni-Ni distances (see Fig. 7).
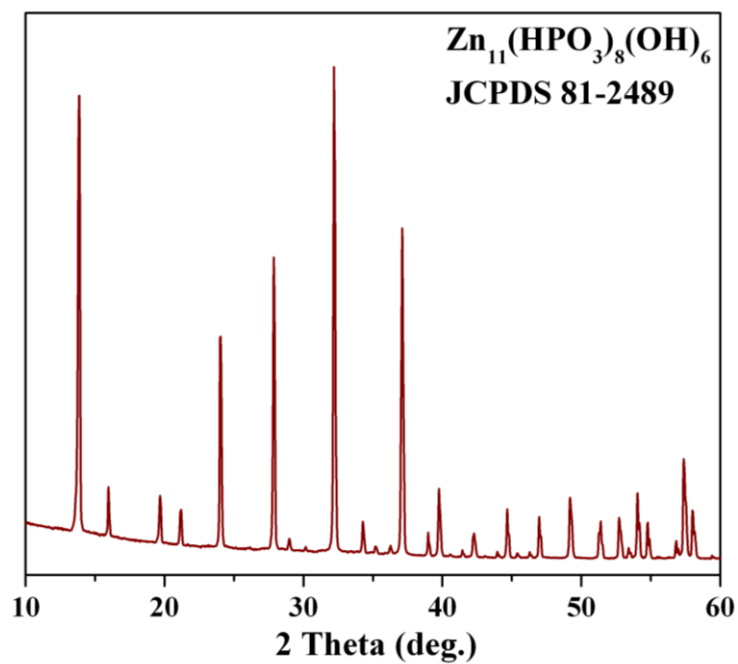
Figure S30. PXRD (in deg) of hexagonal zinc phosphite, $Zn_{11}(HPO_3)_8(OH)_6$ (JCPDS 81-2489) synthesized via a mild hydrothermal approach in similar nickel phosphite (see synthesis section). In addition, the compositions were also confirmed by ICP-AES analysis.
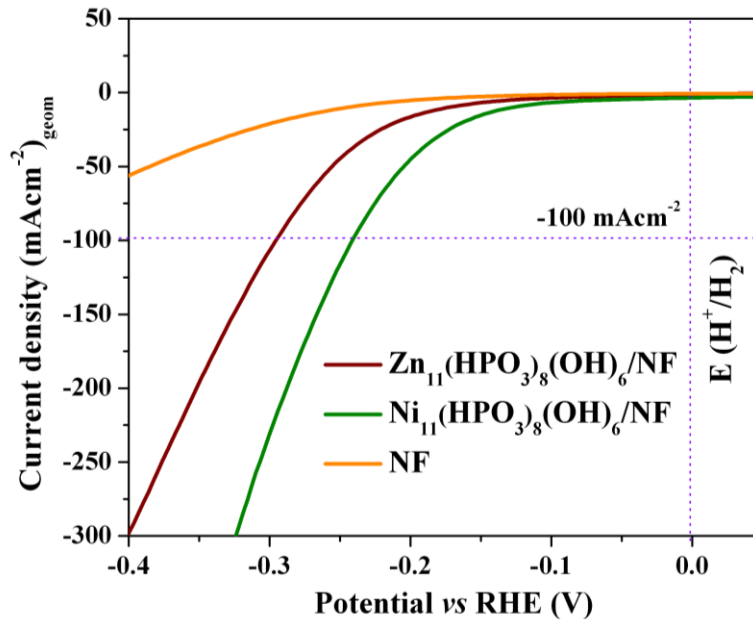
Figure S31. LSV's of Ni$_{11}$(HPO$_3$)$_8$(OH)$_6$ and Zn$_{11}$(HPO$_3$)$_8$(OH)$_6$ deposited on NF and measured with a sweep rate 5 mV/s in 1 M KOH solution (vs RHE). The effective HER activity Zn$_{11}$(HPO$_3$)$_8$(OH)$_6$ indicates the participation of phosphite groups in catalysis.
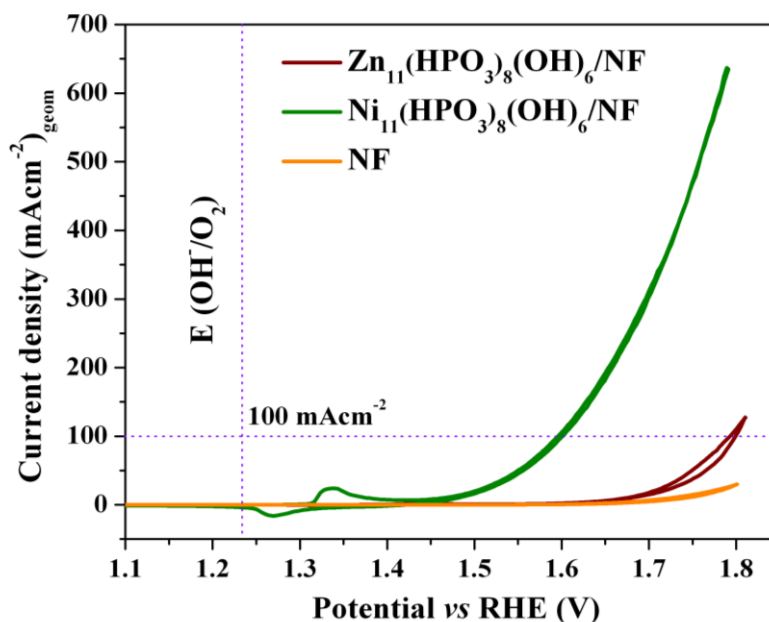

Figure S32. CV's of Ni$_{11}$(HPO$_3$)$_8$(OH)$_6$ and Zn$_{11}$(HPO$_3$)$_8$(OH)$_6$ deposited on NF and measured with a sweep rate 1 mV/s in 1 M KOH solution (vs RHE). The Zn$_{11}$(HPO$_3$)$_8$(OH)$_6$ was clearly less active both in terms of current density and overpotentials, exhibiting the prominent role of Ni in OER catalysis.
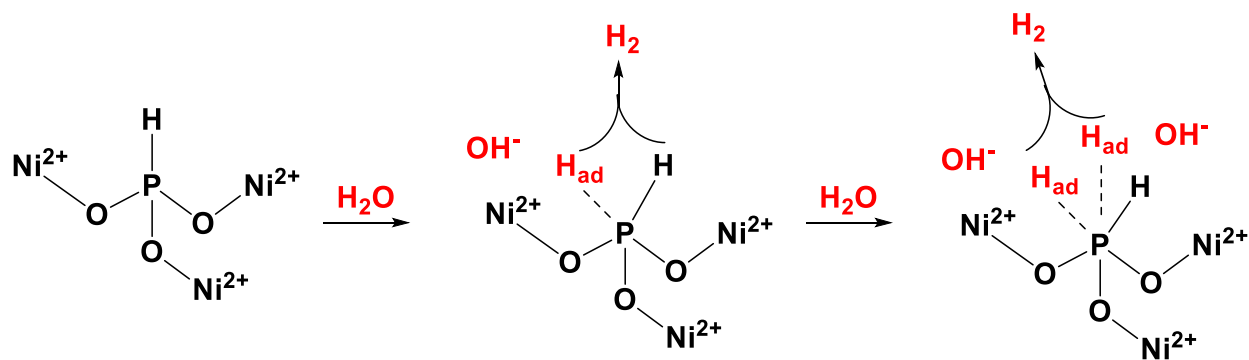
Figure S33. A plausible mechanism of P centred HER catalysis of $Ni_{11}(HPO_3)_8(OH)_6$ leading to H_2 from H_2O. The very first step involves Ni^{2+} based dissociation of H_2O followed by adsorption of eithetr one (middle) and/or two (extreme right) protons at the P centre with subsequent release of H_2.
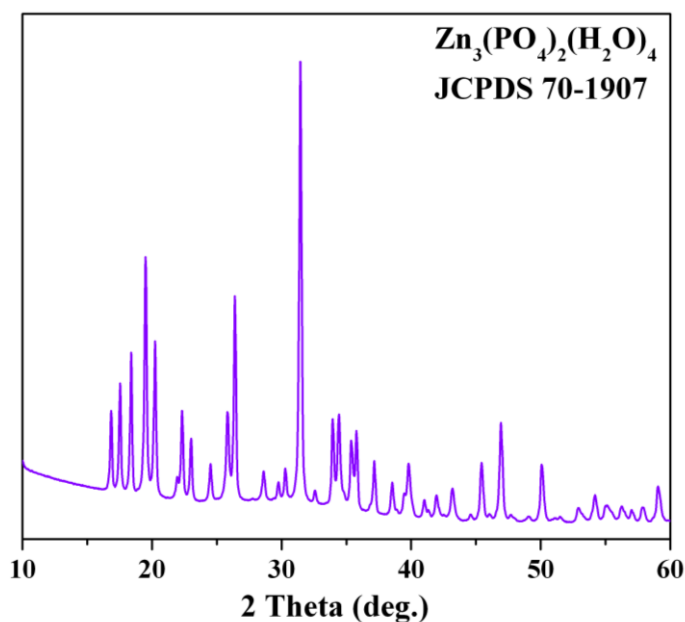

Figure S34. PXRD (in deg) of orthorhombic zinc phosphate, $Zn_3(PO_4)_2(H_2O)_4$ (JCPDS 70-1907) synthesized by precipitation approach (see synthesis section in the main text). In addition, the compositions were also confirmed by ICP-AES analysis.
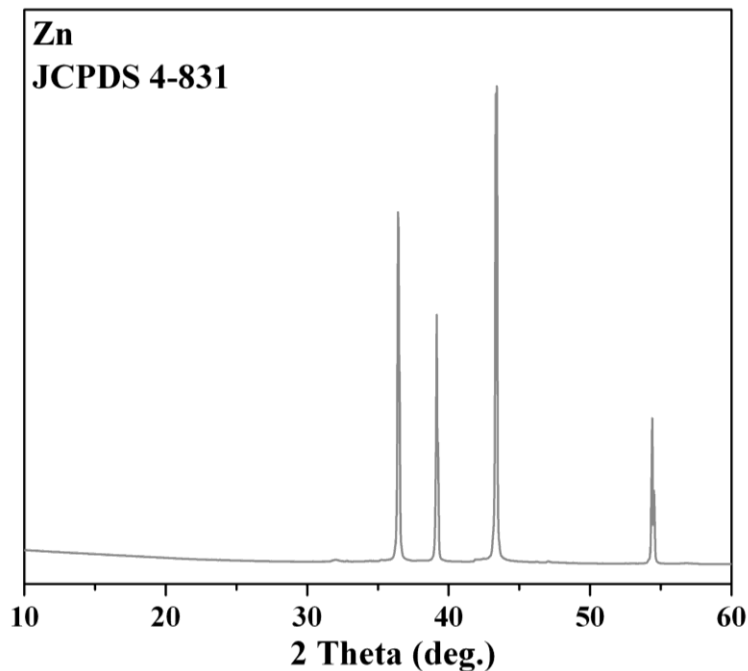
Figure S35. PXRD (in deg) of hexagonal zinc (JCPDS 4-381) which was purchased from Sigma Aldrich.
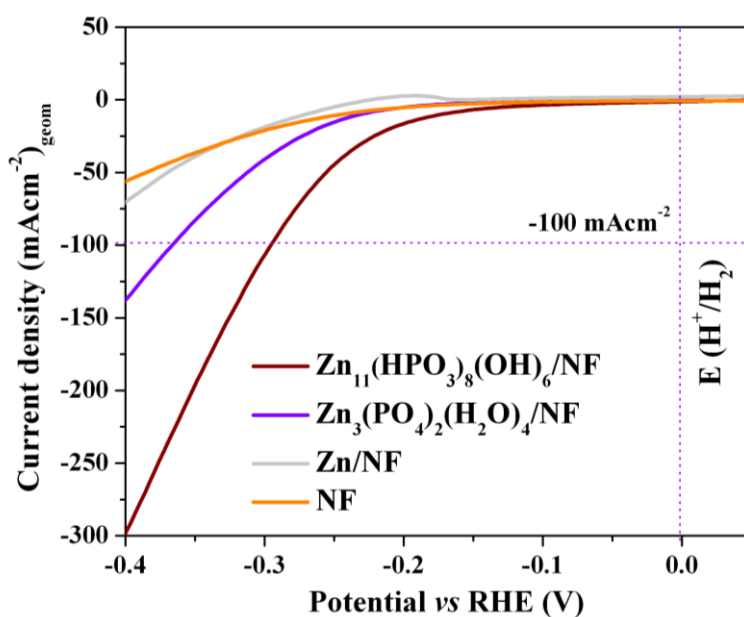

Figure S36. LSV's of $Zn_{11}(HPO_3)_8(OH)_6$, $Zn_3(PO_4)_2(H_2O)_4$ and Zn powder deposited on NF and measured with a sweep rate 5 mV/s in 1 M KOH solution (vs RHE) for HER. The substantially higher catalytic activity of phosphite over phosphate groups and Zn suggest the participation of phosphite in HER.
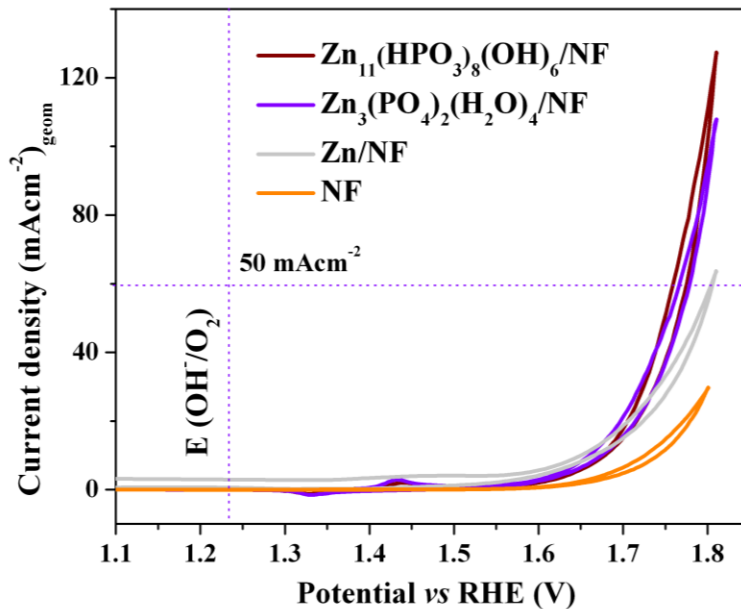
31

Figure S37. CV's of $Zn_{11}(HPO_3)_8(OH)_6$, $Zn_3(PO_4)_2(H_2O)_4$ and Zn powder deposited on NF and measured with a sweep rate 1 mV/s in 1 M KOH solution (vs RHE) for OER. The catalytic activity of all materials was almost close to each other specifying no direct involvement of anions in catalysis.
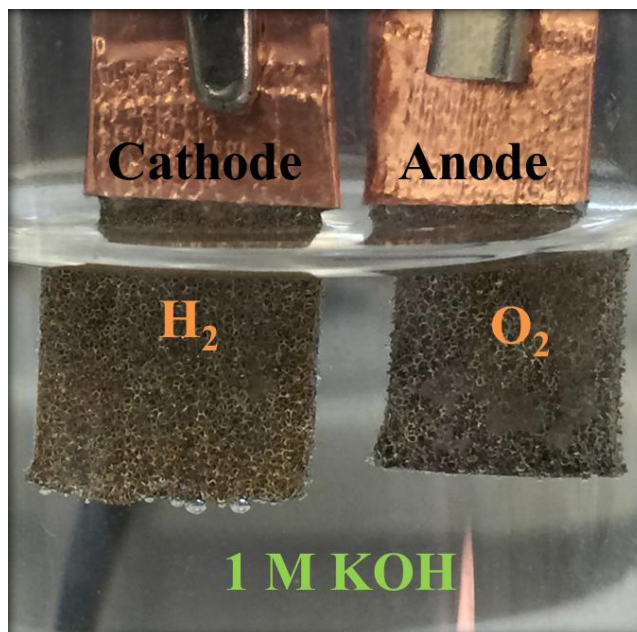

Figure S38. Overall water-splitting with $Ni_{11}(HPO_3)_8(OH)_6 \| Ni_{11}(HPO_3)_8(OH)_6$ on NF in 1 M KOH solution. Vigorous bubble formation was observed during the experiment.

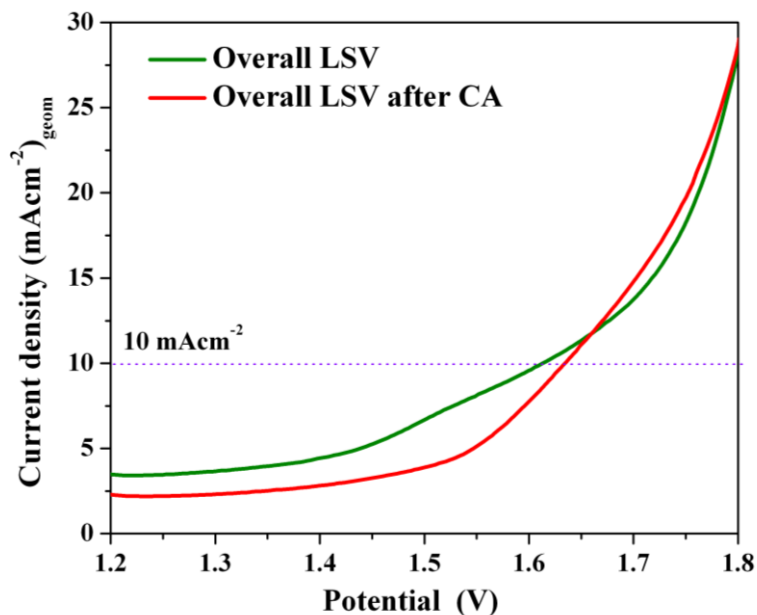**Figure S39.** Comparison of the current–potential plot of an alkaline electrolyzer using $Ni_{11}(HPO_3)_8(OH)_6 \| Ni_{11}(HPO_3)_8(OH)_6$ on NF as both cathode and anode in 1 M KOH solution with a scan rate of 1 mV/s. Similar potentials were obtained at a constant current density of 10 mAcm^{-2} even after the durability tests over 4 days.
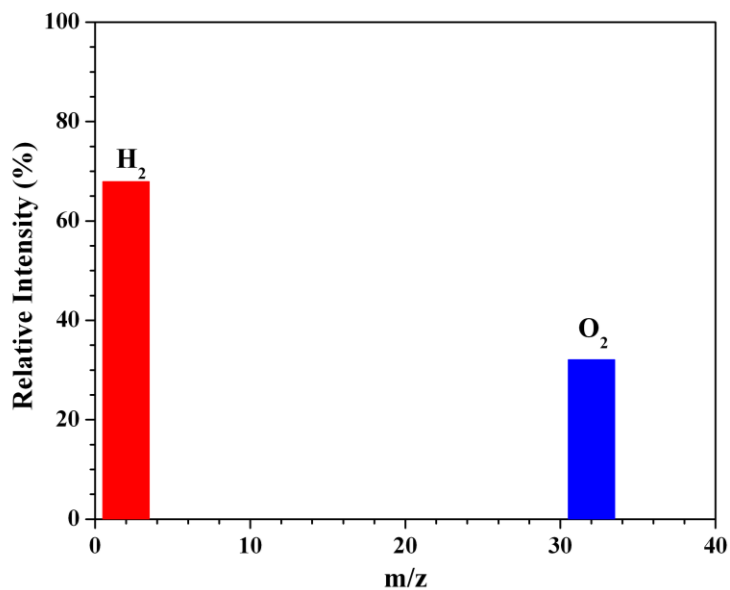

Figure S40. Mass spectrometric analysis of the gas evolved as a result of elelctrolysis of water in a colsed electrochemical cell in 1 M KOH. The relative ratio of H_2 to O_2 was obtained to be ~ 2:1 confirming the selectivity of the nickel phosphite catalyst towards HER and OER.

Calculation of Faradaic efficiency

The Faradaic efficiency (FE) of $Ni_{11}(HPO_3)_8(OH)_6$ in 1M KOH towards oxygen and hydrogen evolution reaction was measured in a two-electrode configuration where nickel foam loaded with $Ni_{11}(HPO_3)_8(OH)_6$ were used as both cathode and anode in a closed electrochemical cell. The electrolyte and cell were first degassed with Argon for 30 min under stirring. Afterwards, constant current density of 10 mAcm^{-2} was applied for a certain period of time. At the end of electrolysis, the gaseous samples were drawn from the head space by a gas tight syringe and analyzed by a GC calibrated for H_2, and O_2. Each injection was repeated at least three times and the average value is presented. Similarly, the FE of the used catalyst after 100 h of CA experiments was also calculated.

The Faradaic efficiency (FE) is calculated based on:

$$FE(H_2, \%) = \frac{V_{H_2} \times 2 \times F}{V_m \times j \times t} \times 100\%$$

$$FE(O_2, \%) = \frac{V_{O_2} \times 4 \times F}{V_m \times j \times t} \times 100\%$$

V_{H2}, V_{O2} is the evolved volume of hydrogen and oxygen, F is the Faraday constant (96485.33289 C/mol), V_m is the molar volume of the gas, j is the current density (10 mAcm^{-2}) and t is the time period of electrolysis.

Table S8: Calculation of Faradaic efficiency

	j /mAcm^{-2}	t/ sec	V_{H2}/ mL	V_{O2}/ mL	V_{H2}:V_{O2}	FE (H_2,%)	FE (O_2,%)
Fresh catalyst	10	480	0.552	0.264	2.1:1	99	95
Catalyst after 4d	10	480	0.529	0.262	2.0:1	95	94
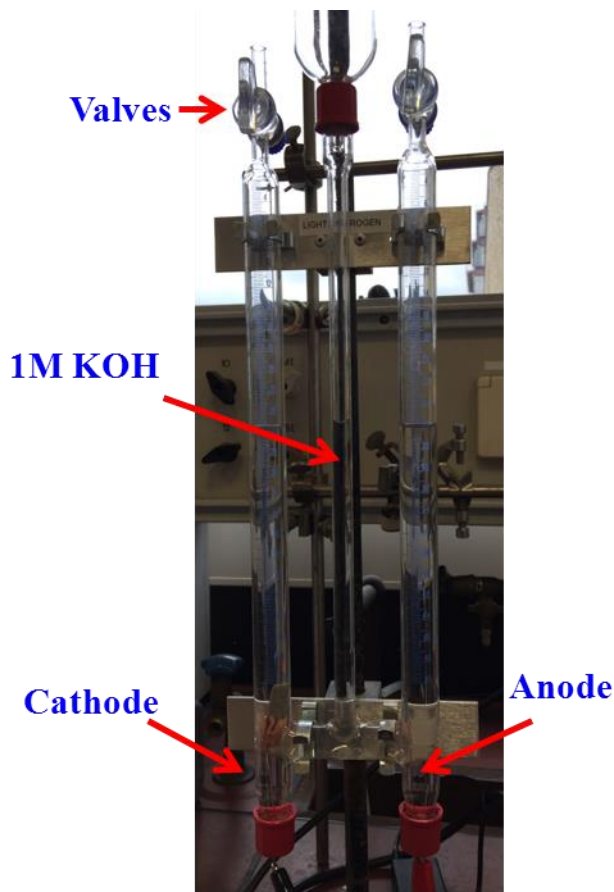
Electrolyzer set-up
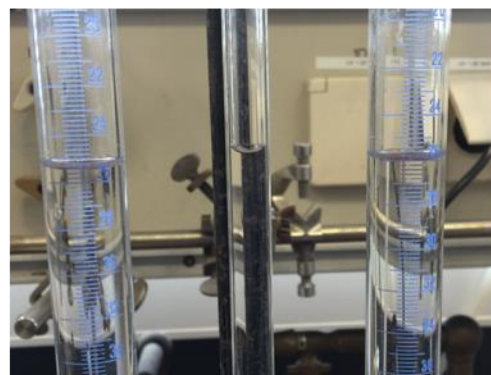
Initial
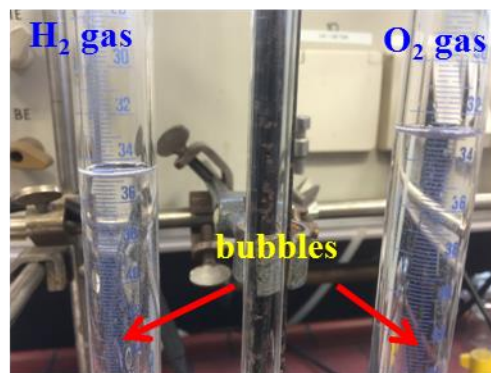
During gas evolution

Figure S41. The electrolysis was performed in a modified two-electrode $Ni_{11}(HPO_3)_8(OH)_6 \| Ni_{11}(HPO_3)_8(OH)$ configuration at a constant current density of 10 mAcm^{-2} in 1 M KOH. An inverted graduated electrochemical cell was constructed to allow collection of H_2 and O_2 separately at atmospheric pressure as shown in the Figure left. First of all, the initial levl of the electrolyte was noted and then the valves were closed (top right). During electrolysis, as a result of evolution and collection of H_2 and O_2 at the upper part of the cell, the level of electrolyte goes down and the change in volume over time is recorded (Figure right). The ratio of volumes of H_2 and O_2 remained almost 2:1 over the period of electrolysis. Similar experiment was also conducted using the electrodes that has been used for 4 days of electrolysis to demonstrate the conservation of the efficiency of the catalyst (Figure S42).
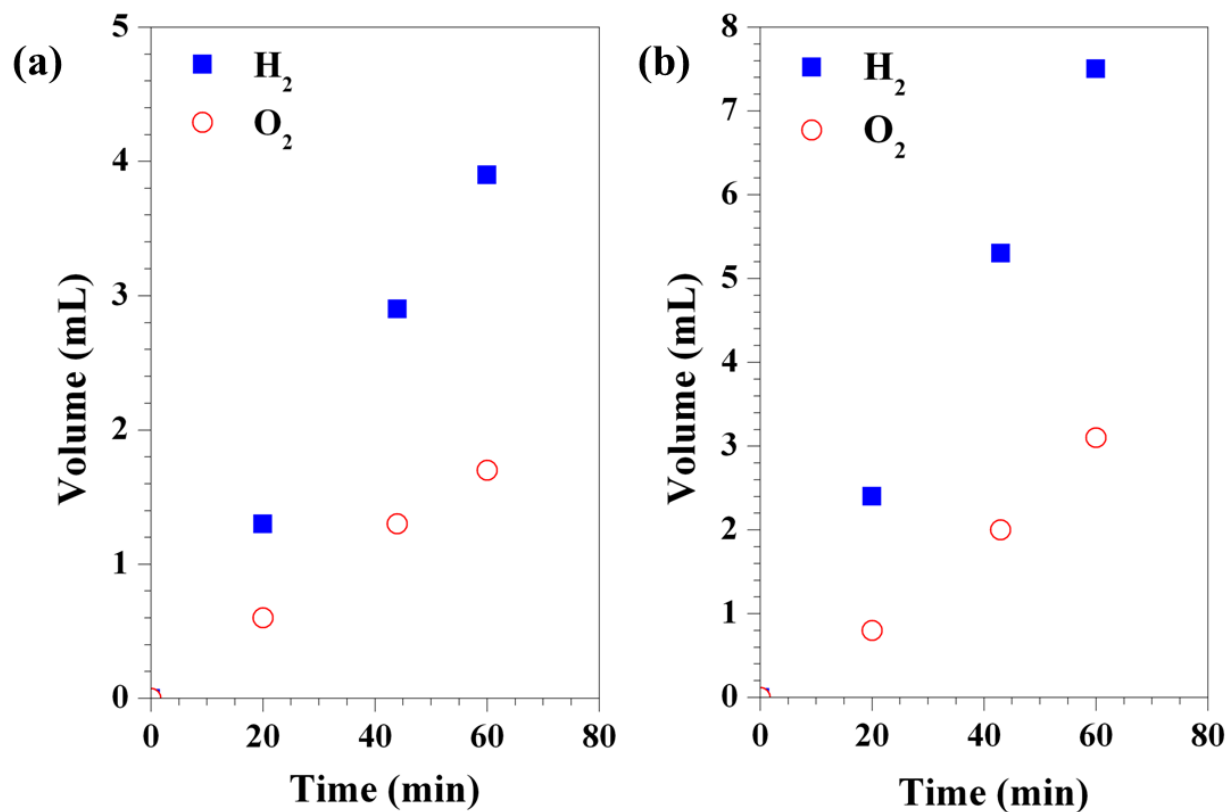
Figure S42. Graph (a) initial; (b).after 4d showing the volume change as result of H_2 and O_2 evolution in the experiments of Figure S41 with respect to time. The ratios of H_2 and O_2 were obtained from the modified two electrode $Ni_{11}(HPO_3)_8(OH)_6 \| Ni_{11}(HPO_3)_8(OH)_6$ on NF as both cathode and anode in 1 M KOH solution at a current of 10 mAcm^{-2} for 1 h. The attained ratios directly confrmed the evolution of gases as well as the amount of H_2 was approximately twice larger than the O_2 demonstrating the effcient selectvity and reactivity of the catalysts.

Figure S43. HR-TEM images (a, b) showing minimum surface changes on the crystalline particles of $Ni_{11}(HPO_3)_8(OH)_6$ after overall water splitting experiments.

References

1. M. D. Marcos, P. Amoros, A. Beltranporter, R. Martinezmanez and J. P. Attfield, *Chem. Mater.*, 1993, **5**, 121-128.
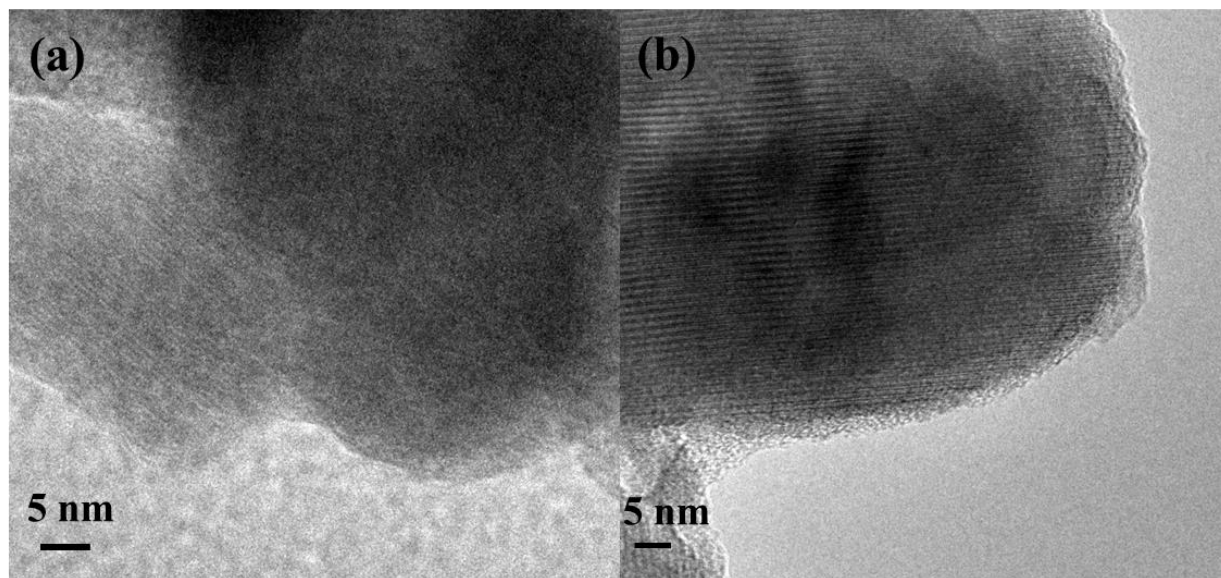2. Y. P. Gao, J. H. Zhao, Z. Run, G. Q. Zhang and H. Pang, *Dalt. Trans.*, 2014, **43**, 17000-17005.
3. H. Pang, C. Z. Wei, Y. H. Ma, S. S. Zhao, G. C. Li, J. S. Zhang, J. Chen and S. J. Li, *ChemPlusChem*, 2013, **78**, 546-553.
4. D. H. Lee, M. Kang, S. M. Paek and H. Jung, *Bull. Korean Chem. Soc.*, 2016, **37**, 192-199.
5. Y. Z. Su, K. Xiao, N. Li, Z. Q. Liu and S. Z. Qiao, *J. Mater. Chem. A*, 2014, **2**, 13845-13853.
6. A. Davidson, J. F. Tempere, M. Che, H. Roulet and G. Dufour, *J. Phys. Chem.*, 1996, **100**, 4919-4929.
7. Y. Zhan, M. H. Lu, S. L. Yang, Z. L. Liu and J. Y. Lee, *ChemElectrochem*, 2016, **3**, 615-621.
8. A. P. Grosvenor, M. C. Biesinger, R. S. Smart and N. S. McIntyre, *Surf. Sci.*, 2006, **600**, 1771-1779.
9. D. U. Lee, J. Fu, M. G. Park, H. Liu, A. G. Kashkooli and Z. W. Chen, *Nano Lett.*, 2016, **16**, 1794-1802.
10. M. C. Biesinger, B. P. Payne, L. W. M. Lau, A. Gerson and R. S. C. Smart, *Surf. Interface Anal.*, 2009, **41**, 324-332.
11. Y. S. Li and Y. L. He, *RSC Advances*, 2014, **4**, 16879-16884.
12. E. L. Ratcliff, J. Meyer, K. X. Steirer, A. Garcia, J. J. Berry, D. S. Ginley, D. C. Olson, A. Kahn and N. R. Armstrong, *Chem. Mater.*, 2011, **23**, 4988-5000.
13. L. Trotochaud, S. L. Young, J. K. Ranney and S. W. Boettcher, *J. Am. Chem. Soc.*, 2014, **136**, 6744-6753.

14. L. Trotochaud, J. K. Ranney, K. N. Williams and S. W. Boettcher, *J. Am. Chem. Soc.*, 2012, **134**, 17253-17261.
15. P. W. Menezes, A. Indra, O. Levy, K. Kailasam, V. Gutkin, J. Pfrommer and M. Driess, *Chem. Commun.*, 2015, **51**, 5005-5008.
16. P. W. Menezes, A. Indra, C. Das, C. Walter, C. Gobel, V. Gutkin, D. Schmeisser and M. Driess, *ACS Catal.* , 2017, **7**, 103-109.
17. H. Q. Zhou, F. Yu, J. Y. Sun, R. He, S. Chen, C. W. Chu and Z. F. Ren, *Proc. Natl. Acad. Sci. U.S.A.*, 2017, **114**, 5607-5611.
18. H. Y. Jin, J. Wang, D. F. Su, Z. Z. Wei, Z. F. Pang and Y. Wang, *J. Am. Chem. Soc.* , 2015, **137**, 2688-2694.
19. Y. S. Jin, H. T. Wang, J. J. Li, X. Yue, Y. J. Han, P. K. Shen and Y. Cui, *Adv. Mater.*, 2016, **28**, 3785-3790.
20. B. M. Hunter, J. D. Blakemore, M. Deimund, H. B. Gray, J. R. Winkler and A. M. Muller, *J. Am. Chem. Soc.*, 2014, **136**, 13118-13121.
21. Y. Rao, Y. Wang, H. Ning, P. Li and M. B. Wu, *ACS Appl. Mater. Interfaces*, 2016, **8**, 33601-33607.
22. X. Y. Yu, Y. Feng, B. Y. Guan, X. W. Lou and U. Paik, *Energy Environ. Sci.*, 2016, **9**, 1246-1250.
23. S. L. Zhao, Y. Wang, J. C. Dong, C. T. He, H. J. Yin, P. F. An, K. Zhao, X. F. Zhang, C. Gao, L. J. Zhang, J. W. Lv, J. X. Wang, J. Q. Zhang, A. M. Khattak, N. A. Khan, Z. X. Wei, J. Zhang, S. Q. Liu, H. J. Zhao and Z. Y. Tang, *Nat. Energy*, 2016, **1**, 1-10.
24. J. J. Duan, S. Chen and C. Zhao, *Nat. Commun.*, 2017, **8**, 15341.
25. A. Han, H. L. Chen, Z. J. Sun, J. Xu and P. W. Du, *Chem. Commun.*, 2015, **51**, 11626-11629.
26. B. You, N. Jiang, M. L. Sheng, M. W. Bhushan and Y. J. Sun, *ACS Catal.*, 2016, **6**, 714-721.
27. Q. Li, Z. C. Xing, D. W. Wang, X. P. Sun and X. R. Yang, *ACS Catal.*, 2016, **6**, 2797-2801.
28. L. A. Stern, L. G. Feng, F. Song and X. L. Hu, *Energy Environ. Sci.*, 2015, **8**, 2347-2351.
29. M. Ledendecker, S. K. Calderon, C. Papp, H. P. Steinruck, M. Antonietti and M. Shalom, *Angew. Chem. Int. Ed.*, 2015, **54**, 12361-12365.
30. N. Jiang, B. You, M. L. Sheng and Y. J. Sun, *ChemCatChem*, 2016, **8**, 106-112.
31. N. Jiang, B. You, M. L. Sheng and Y. J. Sun, *Angew. Chem. Int. Ed.*, 2015, **54**, 6251-6254.
32. F. Song and X. L. Hu, *Nat. Chem.*, 2014, **5**, 4477.
33. H. F. Liang, F. Meng, M. Caban-Acevedo, L. S. Li, A. Forticaux, L. C. Xiu, Z. C. Wang and S. Jin, *Nano Lett.*, 2015, **15**, 1421-1427.
34. Y. G. Li, P. Hasin and Y. Y. Wu, *Adv. Mater.*, 2010, **22**, 1926-1929.
35. L. L. Feng, G. T. Yu, Y. Y. Wu, G. D. Li, H. Li, Y. H. Sun, T. Asefa, W. Chen and X. X. Zou, *J. Am. Chem. Soc.*, 2015, **137**, 14023-14026.
36. X. Y. Lu and C. A. Zhao, *Nat. Commun.*, 2015, **6**.
37. X. Zhang, H. M. Xu, X. X. Li, Y. Y. Li, T. B. Yang and Y. Y. Liang, *ACS Catal.*, 2016, **6**, 580-588.
38. H. Hu, B. Y. Guan, B. Y. Xia and X. W. Lou, *J. Am. Chem. Soc.* , 2015, **137**, 5590-5595.
39. J. X. Feng, S. H. Ye, H. Xu, Y. X. Tong and G. R. Li, *Adv. Mater.*, 2016, **28**, 4698-4703.
40. S. Mao, Z. H. Wen, T. Z. Huang, Y. Hou and J. H. Chen, *Energy Environ. Sci.*, 2014, **7**, 609-616.
41. Y. Liang, Y. Li, H. Wang, J. Zhou, J. Wang, T. Regier and H. Dai, *Nat. Mater.*, 2011, **10**, 780-786.
42. C. C. L. McCrory, S. Jung, J. C. Peters and T. F. Jaramillo, *J. Am. Chem. Soc.* , 2014, **135**, 16977-16987.
43. J. Zhou, Y. B. Dou, A. Zhou, R. M. Guo, M. J. Zhao and J. R. Li, *Adv. Energy Mater.*, 2017, **7**.
44. J. Masud, S. Umapathi, N. Ashokaan and M. Nath, *J. Mater. Chem. A*, 2016, **4**, 9750-9754.

45. H. Li, C. Tsai, A. L. Koh, L. L. Cai, A. W. Contryman, A. H. Fragapane, J. H. Zhao, H. S. Han, H. C. Manoharan, F. Abild-Pedersen, J. K. Norskov and X. L. Zheng, *Nat. Mater.*, 2016, **15**, 48-53.
46. Z. P. Shi, Y. X. Wang, H. L. Lin, H. B. Zhang, M. K. Shen, S. H. Xie, Y. H. Zhang, Q. S. Gao and Y. Tang, *J. Mater. Chem. A*, 2016, **4**, 6006-6013.
47. H. Vrubel and X. L. Hu, *Angew. Chem. Int. Ed.*, 2012, **51**, 12703-12706.
48. Y. J. Sun, C. Liu, D. C. Grauer, J. K. Yano, J. R. Long, P. D. Yang and C. J. Chang, *J. Am. Chem. Soc.*, 2013, **135**, 17699-17702.
49. C. L. Fan, D. L. Piron, A. Sleb and P. Paradis, *J. Electrochem. Soc.*, 1994, **141**, 382-387.
50. M. S. Faber, R. Dziedzic, M. A. Lukowski, N. S. Kaiser, Q. Ding and S. Jin, *J. Am. Chem. Soc.*, 2014, **136**, 10053-10061.
51. H. W. Liang, S. Bruller, R. H. Dong, J. Zhang, X. L. Feng and K. Mullen, *Nat. Commun.*, 2015, **6**, 7992.
52. L. Liao, S. N. Wang, J. J. Xiao, X. J. Bian, Y. H. Zhang, M. D. Scanlon, X. L. Hu, Y. Tang, B. H. Liu and H. H. Girault, *Energy Environ. Sci.*, 2014, **7**, 387-392.
53. C. Hu, Q. Ma, S.-F. Hung, Z.-N. Chen, D. Ou, B. Ren, H. M. Chen, G. Fu and N. Zheng, *Chem*, 2017, **3**, 122-133.
54. Z. Y. Yu, Y. Duan, M. R. Gao, C. C. Lang, Y. R. Zheng and S. H. Yu, *Chem. Sci.* , 2017, **8**, 968-973.
55. M. Y. Zheng, J. Du, B. P. Hou and C. L. Xu, *ACS Appl. Mater. Inter.*, 2017, **9**, 26066-26076.
56. C. C. Du, M. X. Shang, J. X. Mao and W. B. Song, *J. Mater. Chem. A*, 2017, **5**, 15940-15949.
57. L. Fang, W. X. Li, Y. X. Guan, Y. Y. Feng, H. J. Zhang, S. L. Wang and Y. Wang, *Adv. Funct. Mater.*, 2017, **27**.
58. R. Zhang, P. A. Russo, M. Feist, P. Amsalem, N. Koch and N. Pinna, *ACS Appl. Mater. Inter.*, 2017, **9**, 14013-14022.
59. E. J. Popczun, J. R. McKone, C. G. Read, A. J. Biacchi, A. M. Wiltrout, N. S. Lewis and R. E. Schaak, *J. Am. Chem. Soc.* , 2013, **135**, 9267-9270.
60. J. Luo, J.-H. Im, M. T. Mayer, M. Schreier, M. K. Nazeeruddin, N.-G. Park, S. D. Tilley, H. J. Fan and M. Gratzel, *Science*, 2014, **345**, 1593-1596.
61. Q. C. Dong, C. C. Sun, Z. Y. Dai, X. X. Zang and X. C. Dong, *ChemCatChem*, 2016, **8**, 3484-3489.
62. L. G. Feng, H. Vrubel, M. Bensimon and X. L. Hu, *Phys. Chem. Chem. Phys.* , 2014, **16**, 5917-5921.
63. D. N. Liu, Q. Lu, Y. L. Luo, X. P. Sun and A. M. Asiri, *Nanoscale*, 2015, **7**, 15122-15126.
64. X. X. Zou, X. X. Huang, A. Goswami, R. Silva, B. R. Sathe, E. Mikmekova and T. Asefa, *Angew. Chem. Int. Ed.*, 2014, **53**, 4372-4376.
65. J. Q. Tian, Q. Liu, A. M. Asiri and X. P. Sun, *J. Am. Chem. Soc.*, 2014, **136**, 7587-7590.
66. H. B. Wu, B. Y. Xia, L. Yu, X. Y. Yu and X. W. Lou, *Nat. Chem.*, 2015, **6**, 6512.
67. H. W. Nesbitt, D. Legrand and G. M. Bancroft, *Phys. Chem. Minerals*, 2000, **27**, 357-366.
68. P. M. A. Sherwood, *Sur. Sci. Spectra*, 2002, **9**, 62-66.
69. Y. J. Zhang, M. B. Zheng, M. J. Qu, M. J. Sun and H. Pang, *J Alloys Compd.*, 2015, **651**, 214-221.
70. D. Shevchenko, M. F. Anderlund, S. Styring, H. Dau, I. Zaharieva and A. Thapper, *Phys. Chem. Chem. Phys.*, 2014, **16**, 11965-11975.
71. I. Zaharieva, D. Gonzalez-Flores, B. Asfari, C. Pasquini, M. R. Mohammadi, K. Klingan, I. Zizak, S. Loos, P. Chernev and H. Dau, *Energy Env. Sci.*, 2016, **9**, 2433-2443.
72. I. Zaharieva, P. Chernev, M. Risch, K. Klingan, M. Kohlhoff, A. Fischer and H. Dau, *Energy Environ. Sci.*, 2012, **5**, 7081-7089.
73. M. Risch, F. Ringleb, M. Kohlhoff, P. Bogdanoff, P. Chernev, I. Zaharieva and H. Dau, *Energy Environ. Sci.*, 2015, **8**, 661-674.

74. A. Bergmann, I. Zaharieva, H. Dau and P. Strasser, *Energy Environ. Sci.*, 2013, **6**, 2745-2755.
75. A. Bergmann, E. Martinez-Moreno, D. Teschner, P. Chernev, M. Gliech, J. F. de Araujo, T. Reier, H. Dau and P. Strasser, *Nat. Commun.*, 2015, **6**, 8625.